Electronic Supplementary Information (ESI) for:

High denticity oxinate-linear-backbone chelating ligand for diagnostic radiometal ions $[^{111}\text{In}]\text{In}^{3+}$ and $[^{89}\text{Zr}]\text{Zr}^{4+}$

Lily Southcott[a,b], *Xiaozhu Wang*[a], *Luke Wharton*[a,b], *Hua Yang*[b], *Valery Radchenko*[b,c], *Manja Kubeil*[d], *Holger Stephan*[d], *María de Guadalupe Jaraquemada-Peláez*[a]* *and Chris Orvig*[a]*

[a] Medicinal Inorganic Chemistry Group, Department of Chemistry, University of British Columbia, 2036 Main Mall, Vancouver, British Columbia V6T 1Z1, Canada
E-mails: orvig@chem.ubc.ca; mdgjara@chem.ubc.ca

[b] Life Sciences Division, TRIUMF, 4004 Wesbrook Mall, Vancouver, British Columbia, V6T 2A3, Canada

[c] Department of Chemistry, University of British Columbia, 2036 Main Mall, Vancouver, British Columbia V6T 1Z1, Canada

[d] Institute of Radiopharmaceutical Cancer Research, Helmholtz-Zentrum Dresden Rossendorf, Bautzner Landstrasse 400, 01328 Dresden, Germany

*Corresponding Authors: Chris Orvig (orvig@chem.ubc.ca) and María de Guadalupe Jaraquemada-Peláez (mdgjara@chem.ubc.ca)

Table of Contents

NMR spectra of compounds 2 – 7

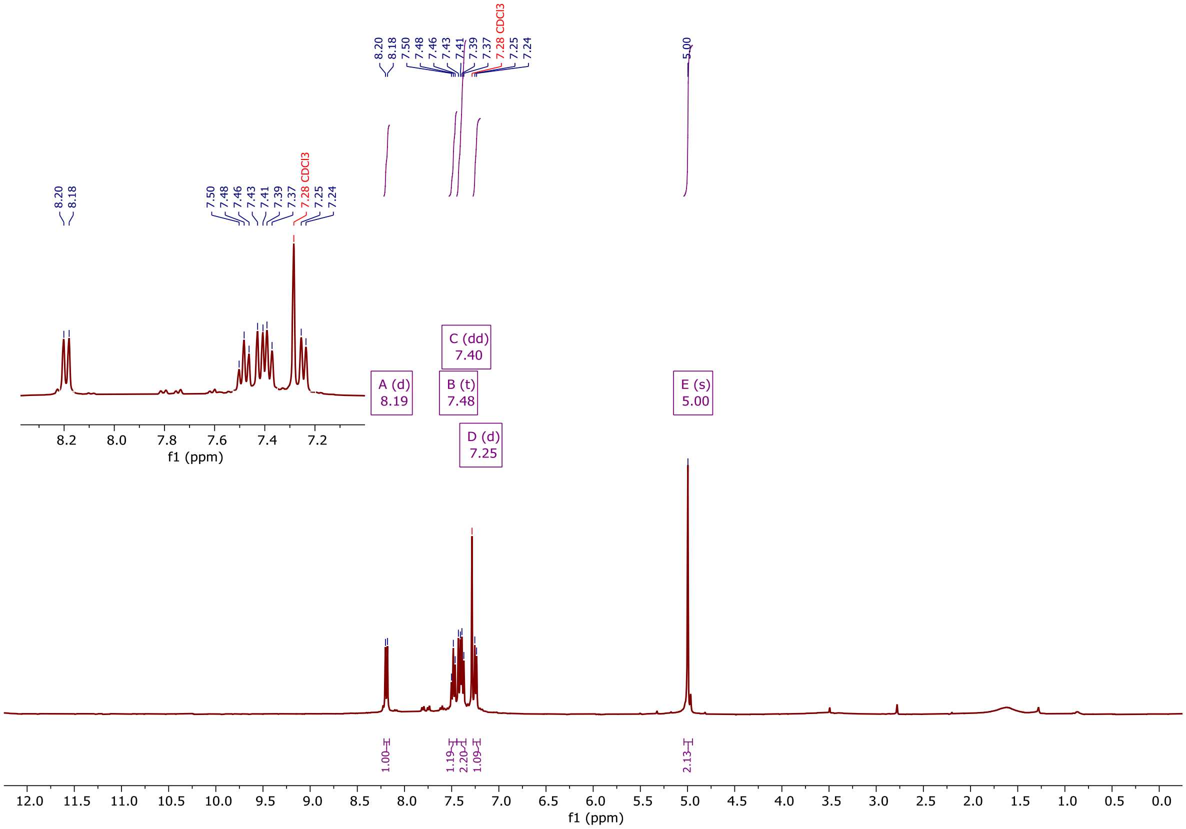

Figure S1. ^{1}H NMR spectrum (CDCl$_3$, RT, 400 MHz) of 2-(hydroxymethyl)quinolin-8-ol **(2)**.

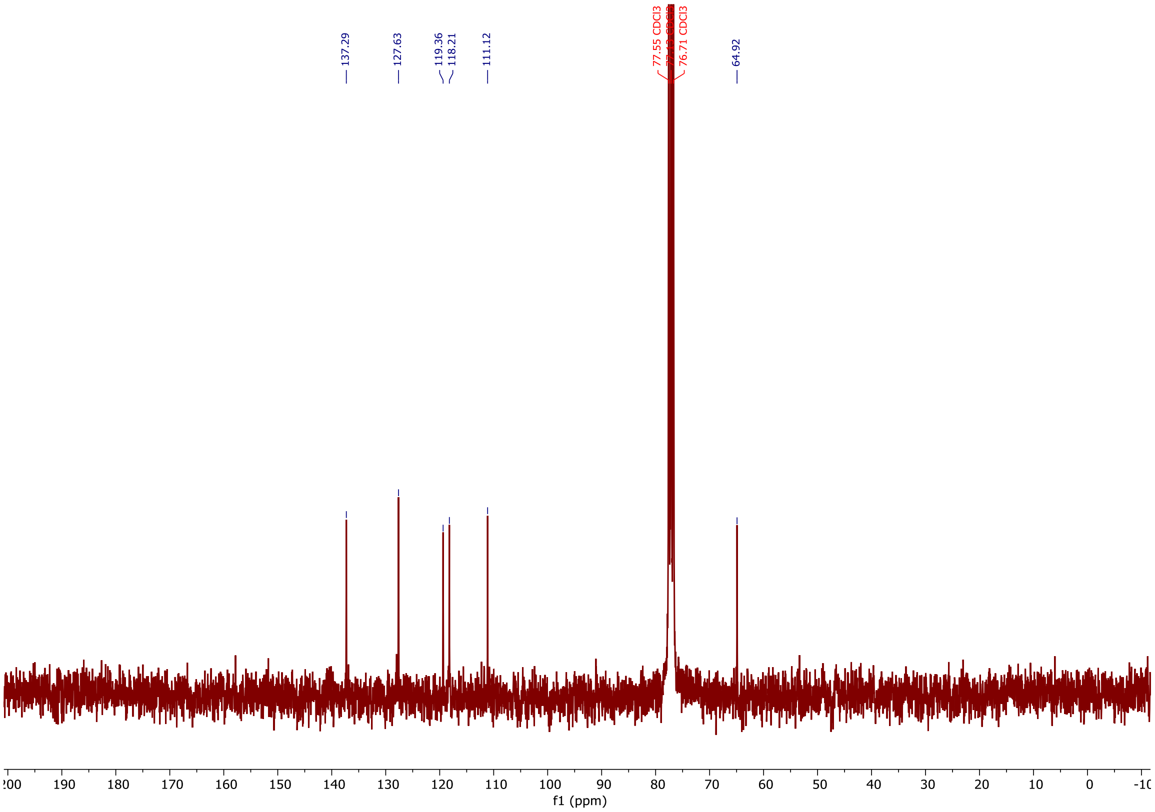

Figure S2. ^{13}C{^{1}H} NMR spectrum (CDCl$_3$, RT, 75 MHz) of 2-(hydroxymethyl)quinolin-8-ol **(2)**.

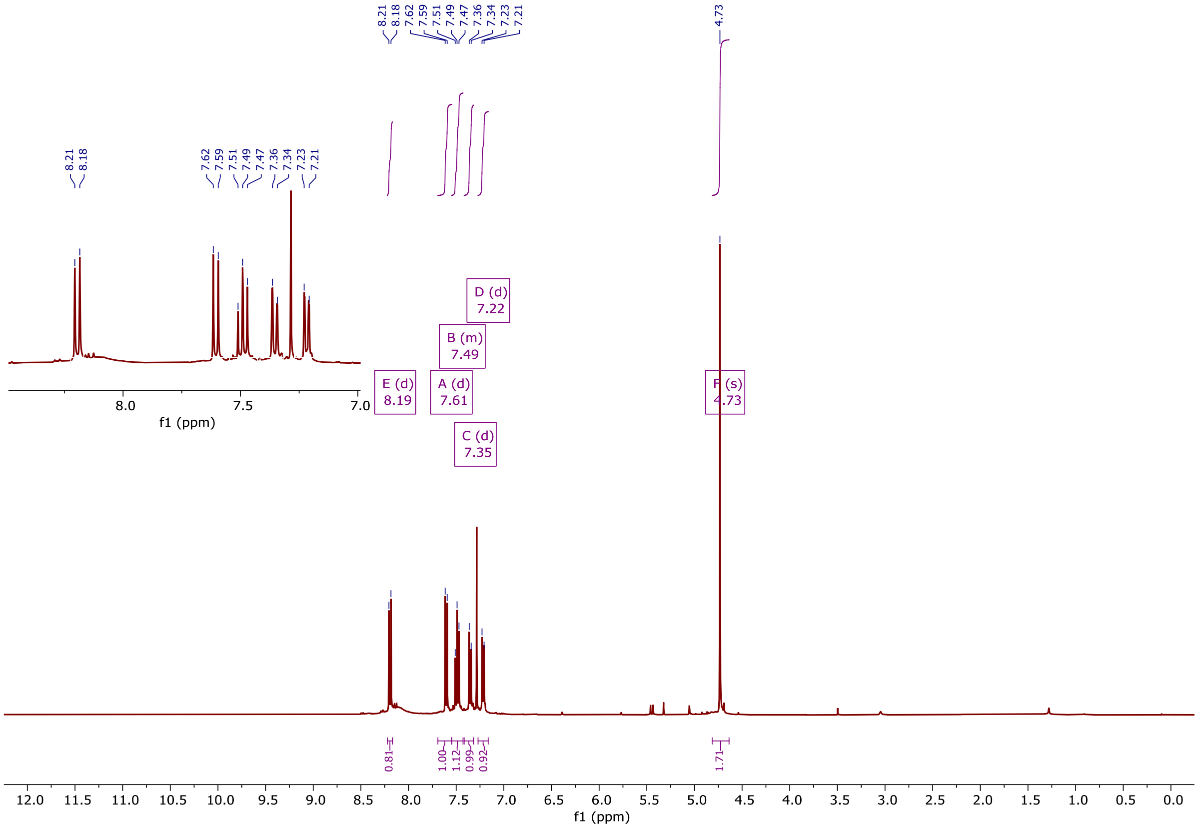

Figure S3. ^{1}H NMR spectrum ($CDCl_3$, RT, 400 MHz) of 2-(bromomethyl)quinoline-8-ol **(3)**.

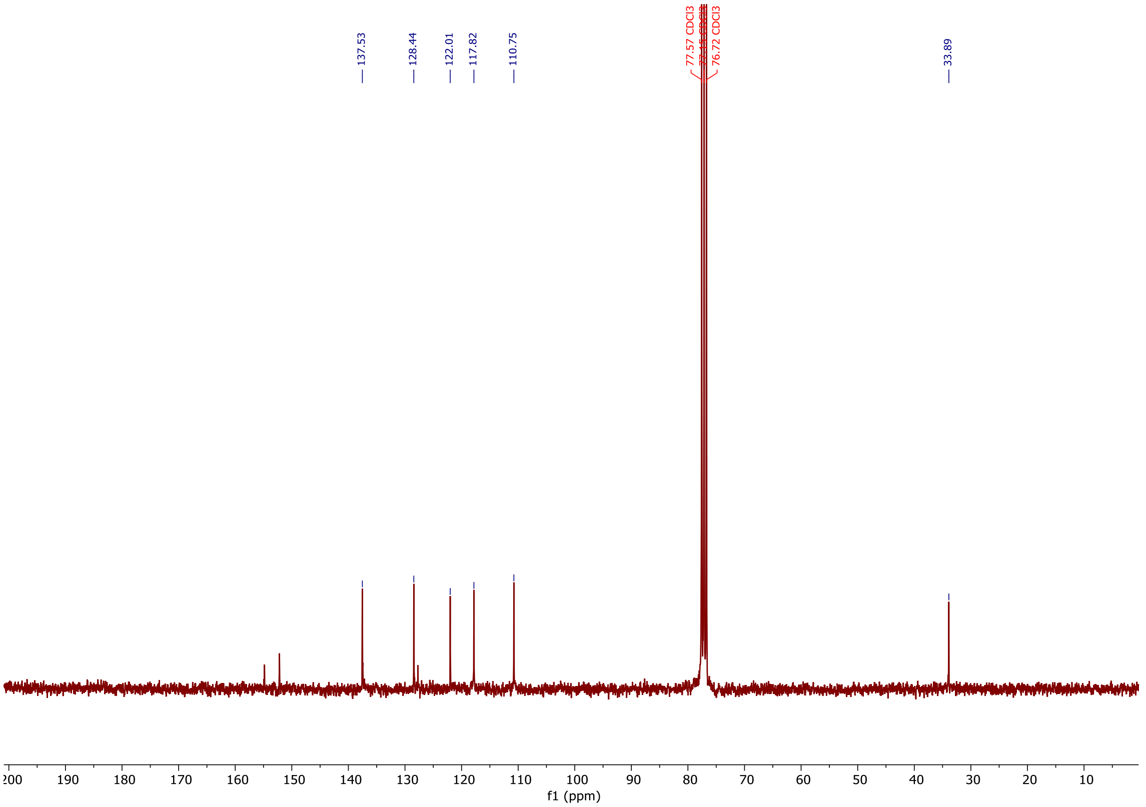

Figure S4. $^{13}C\{^{1}H\}$ NMR spectrum ($CDCl_3$, RT, 100 MHz) of 2-(bromomethyl)quinoline-8-ol **(3).**

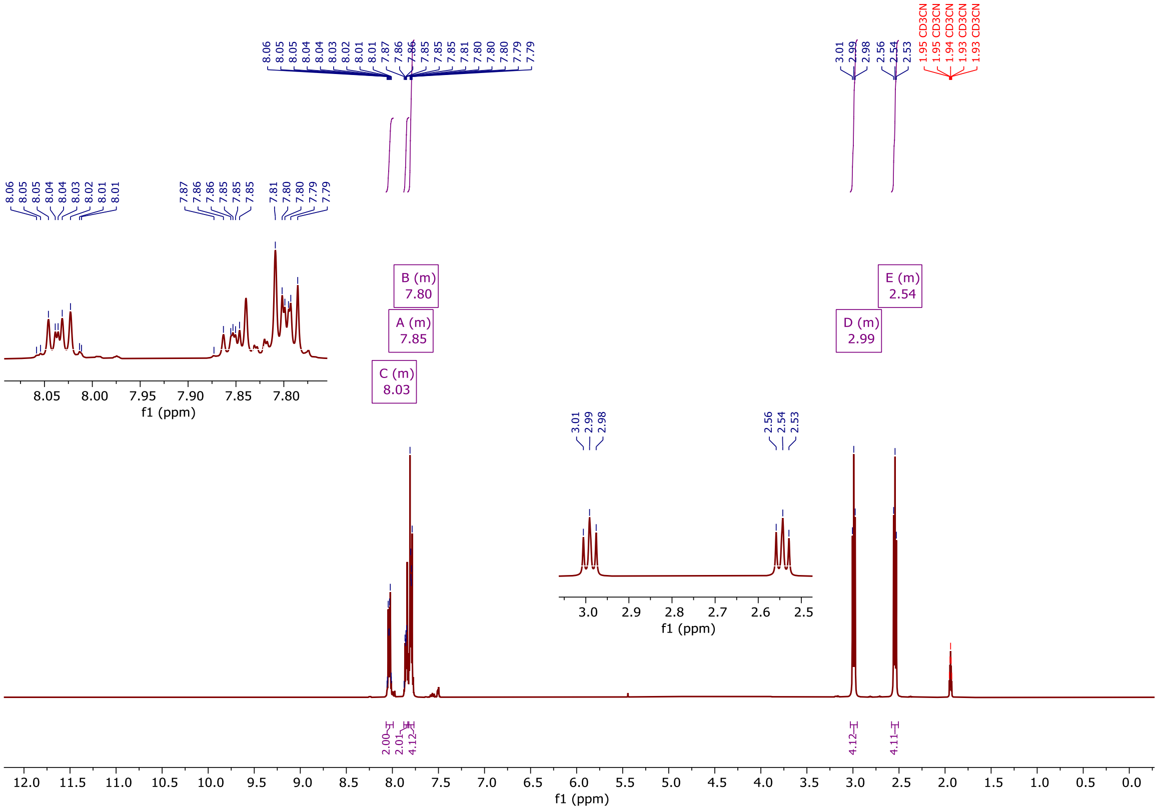

Figure S5. ^{1}H NMR spectrum (CD_3CN, RT, 400 MHz) of *N,N'*-(2-nitrobenzensulfonamide)-1,2-triaminodiethane **(4).**

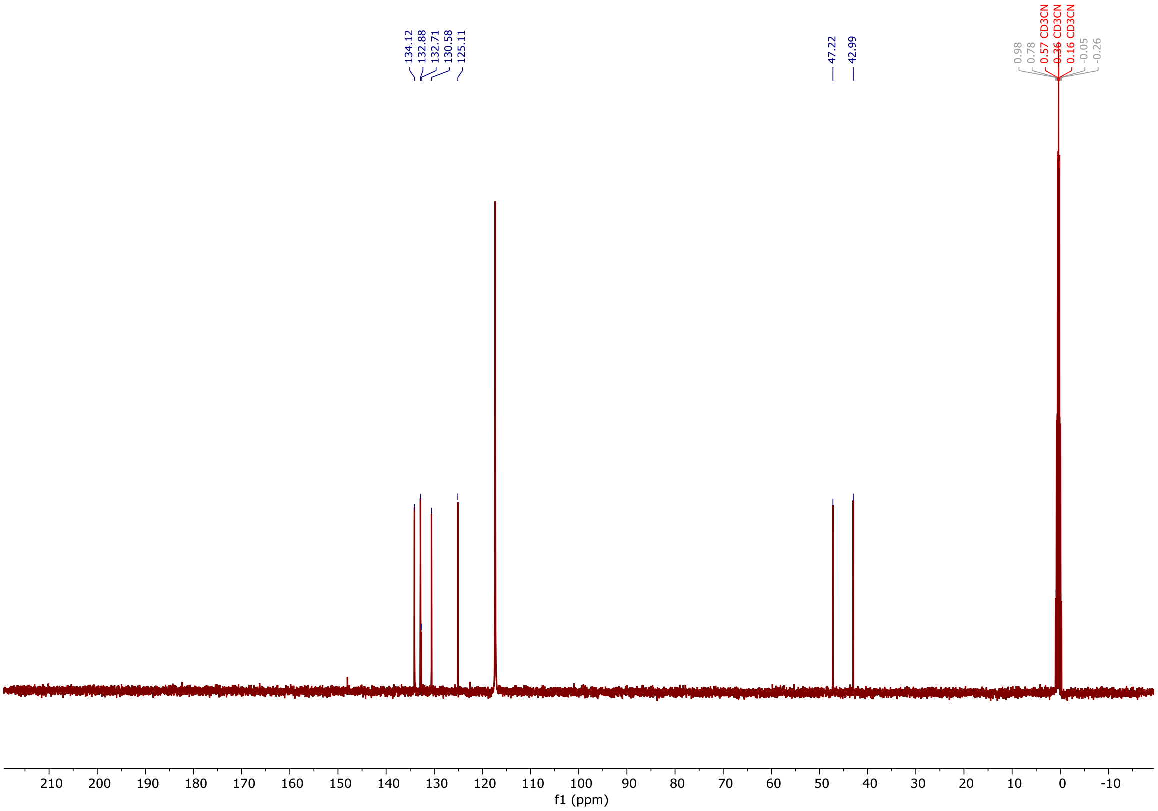

Figure S6. $^{13}C\{^1H\}$ NMR spectrum (CD_3CN, RT, 100 MHz) of *N,N'*-(2-nitrobenzensulfonamide)-1,2-triaminodiethane **(4).**

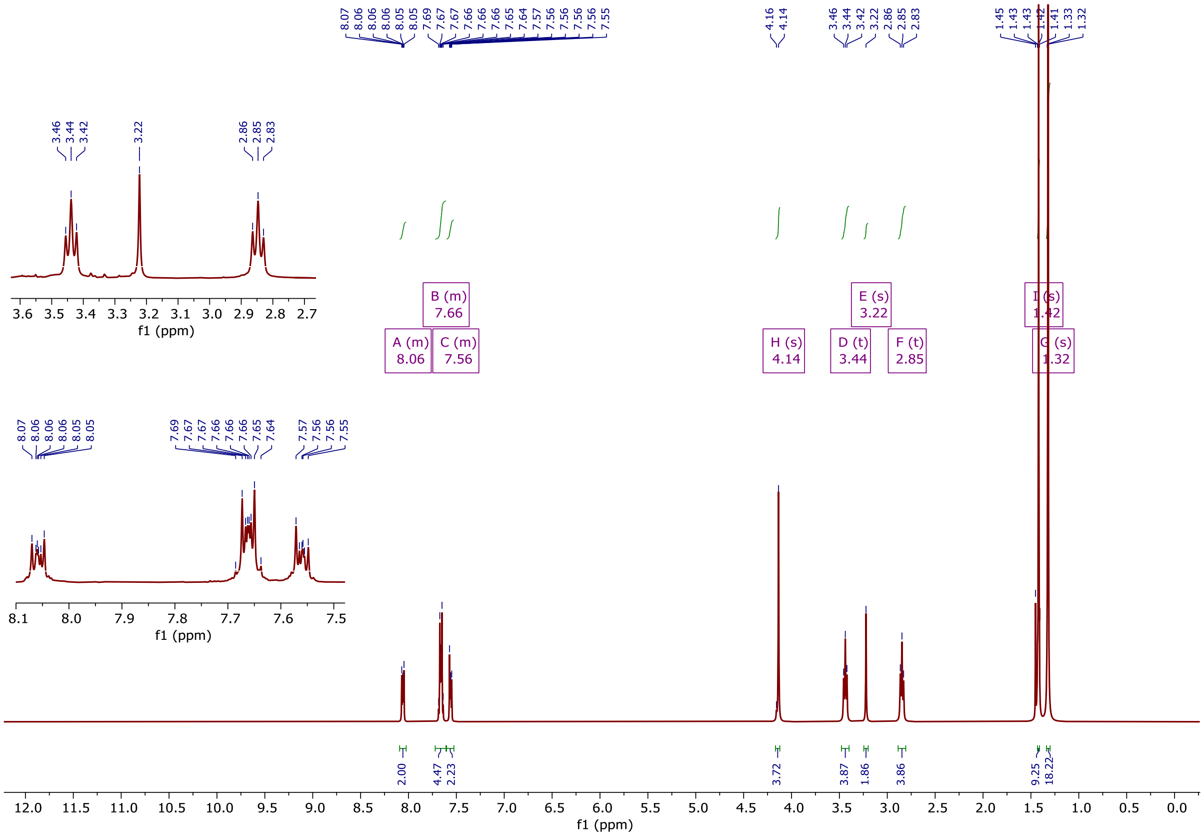

Figure S7. ^{1}H NMR spectrum ($CDCl_3$, RT, 400 MHz) of di-tert-butyl2,2'-((((2-(tert-butoxy)-2-oxoethyl)azanediyl)bis(ethane-2,1-diyl))bis((phenylsulfonyl)azanediyl))diacetate **(5).**

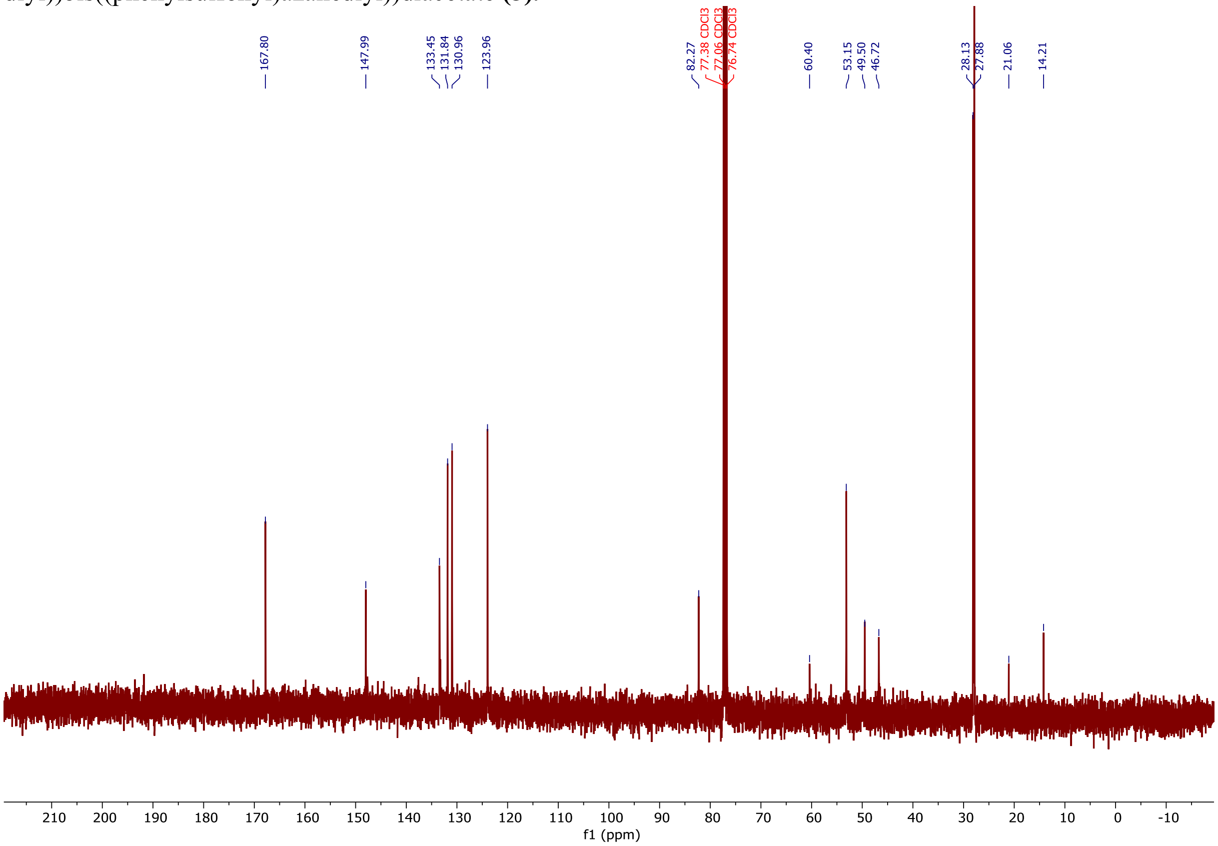

Figure S8. $^{13}C\{^{1}H\}$ NMR spectrum ($CDCl_3$, RT, 100 MHz) of di-tert-butyl2,2'-((((2-(tert-butoxy)-2-oxoethyl)azanediyl)bis(ethane-2,1-diyl))bis((phenylsulfonyl)azanediyl))diacetate **(5).**

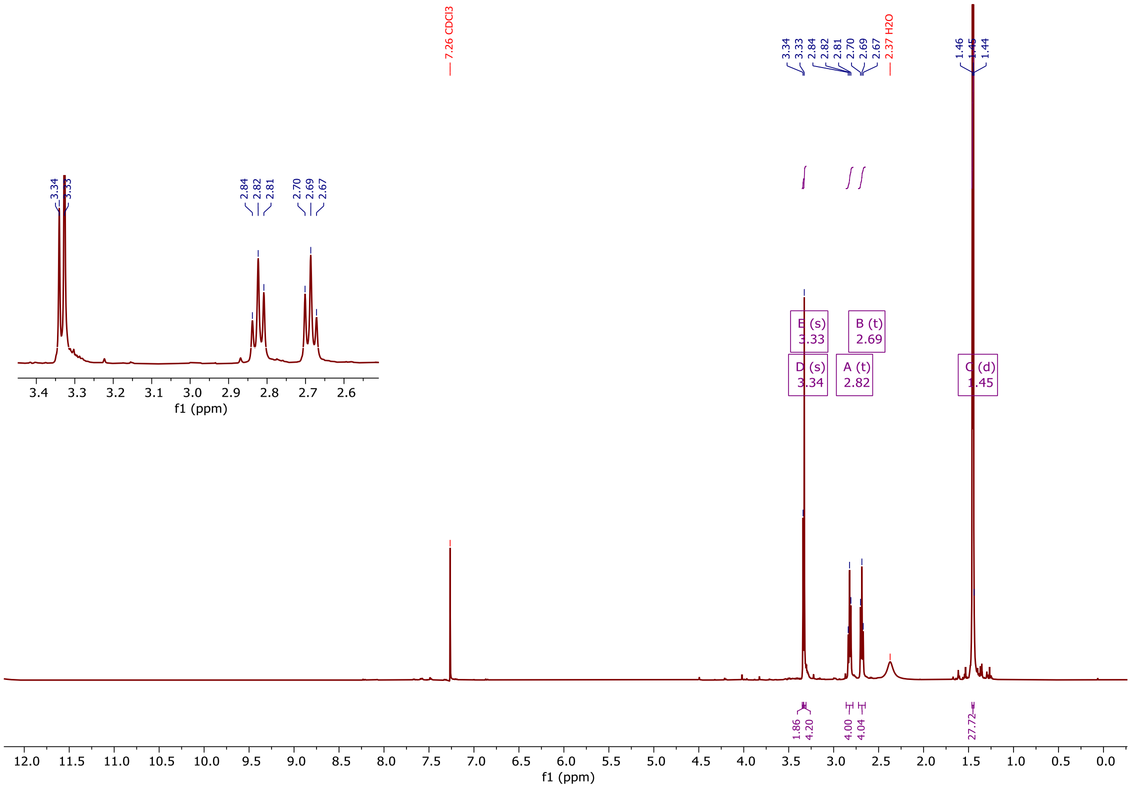

Figure S9. ^{1}H NMR spectrum ($CDCl_3$, RT, 400 MHz) of di-tert-butyl 2,2'-((((2-(tert-butoxy)-2-oxoethyl)azanediyl)bis(ethane-2,1-diyl))bis(azanediyl))diacetate **(6).**

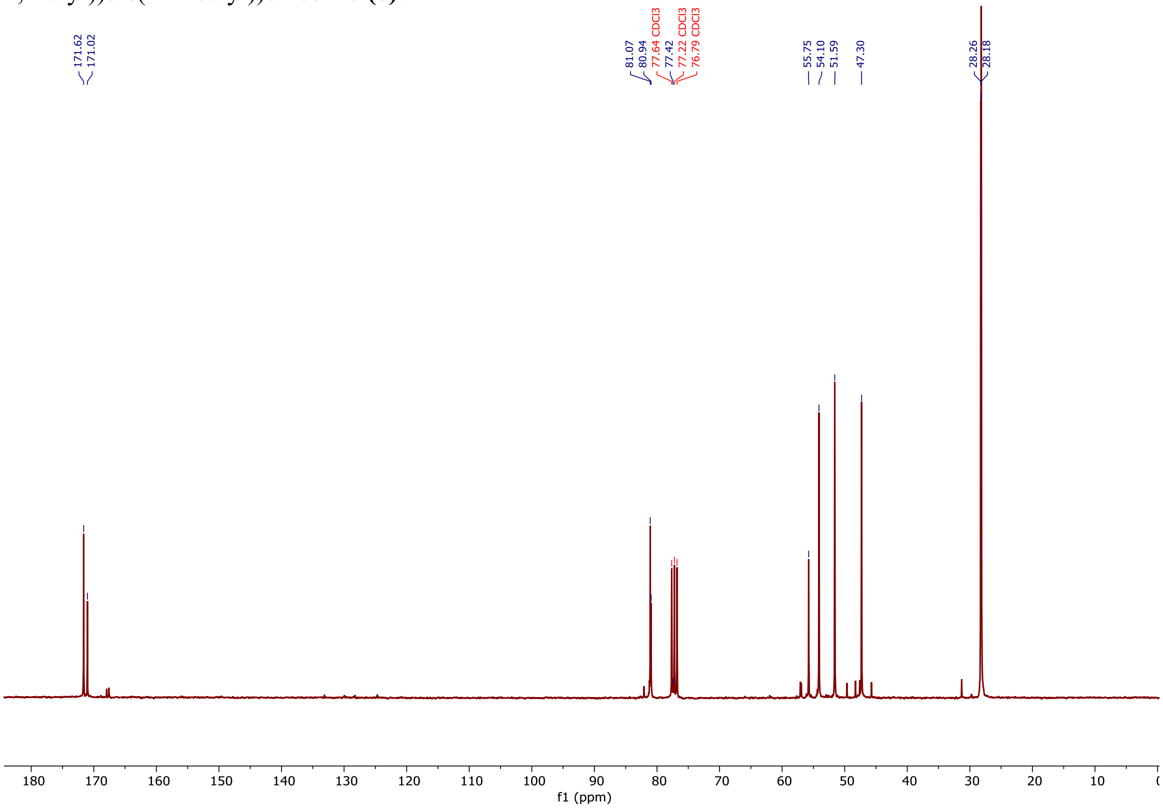

Figure S10. $^{13}C\{^{1}H\}$ NMR spectrum ($CDCl_3$, RT, 100 MHz) of di-tert-butyl 2,2'-((((2-(tert-butoxy)-2-oxoethyl)azanediyl)bis(ethane-2,1-diyl))bis(azanediyl))diacetate **(6).**

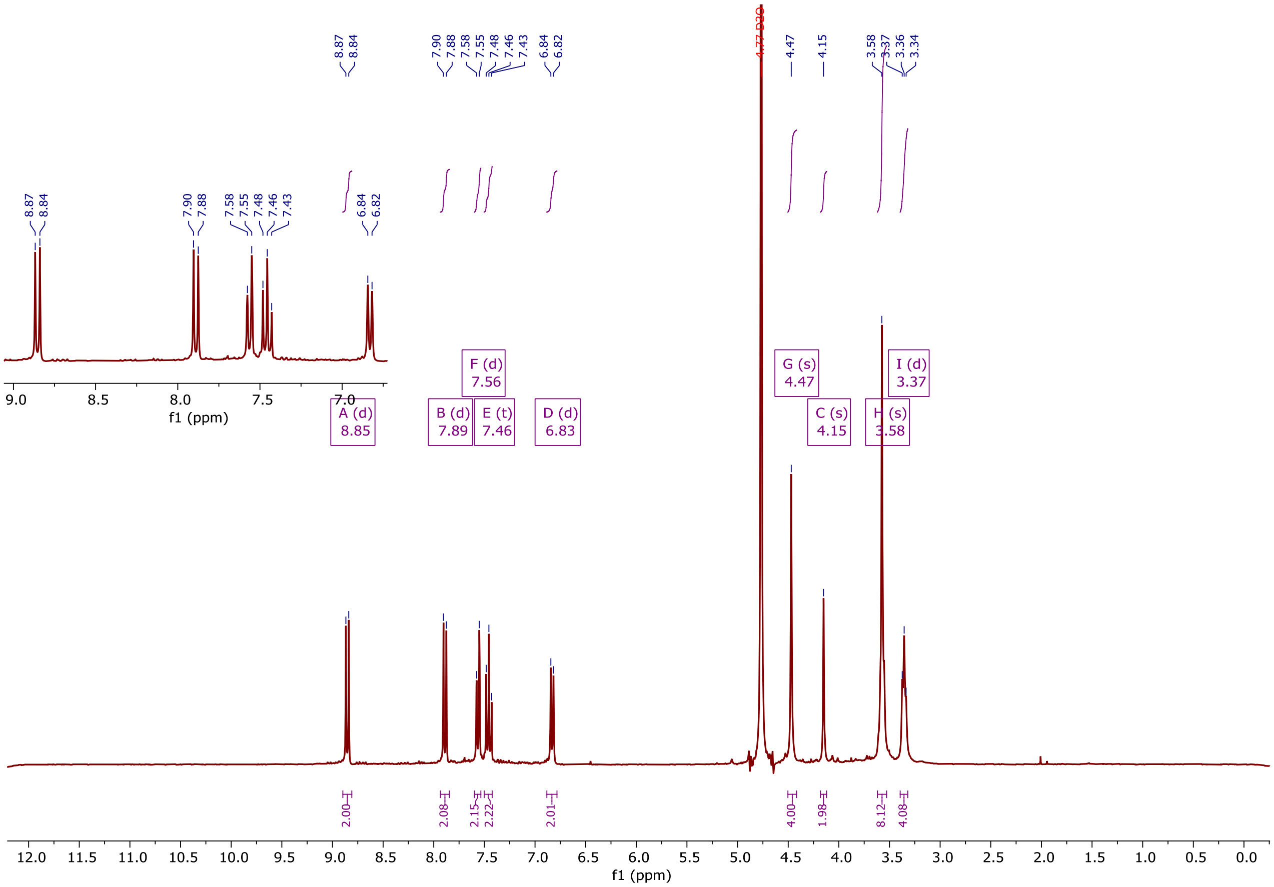

Figure S11. ^{1}H NMR spectrum (D_2O, RT, 300 MHz) of H_5decaox **(7).**

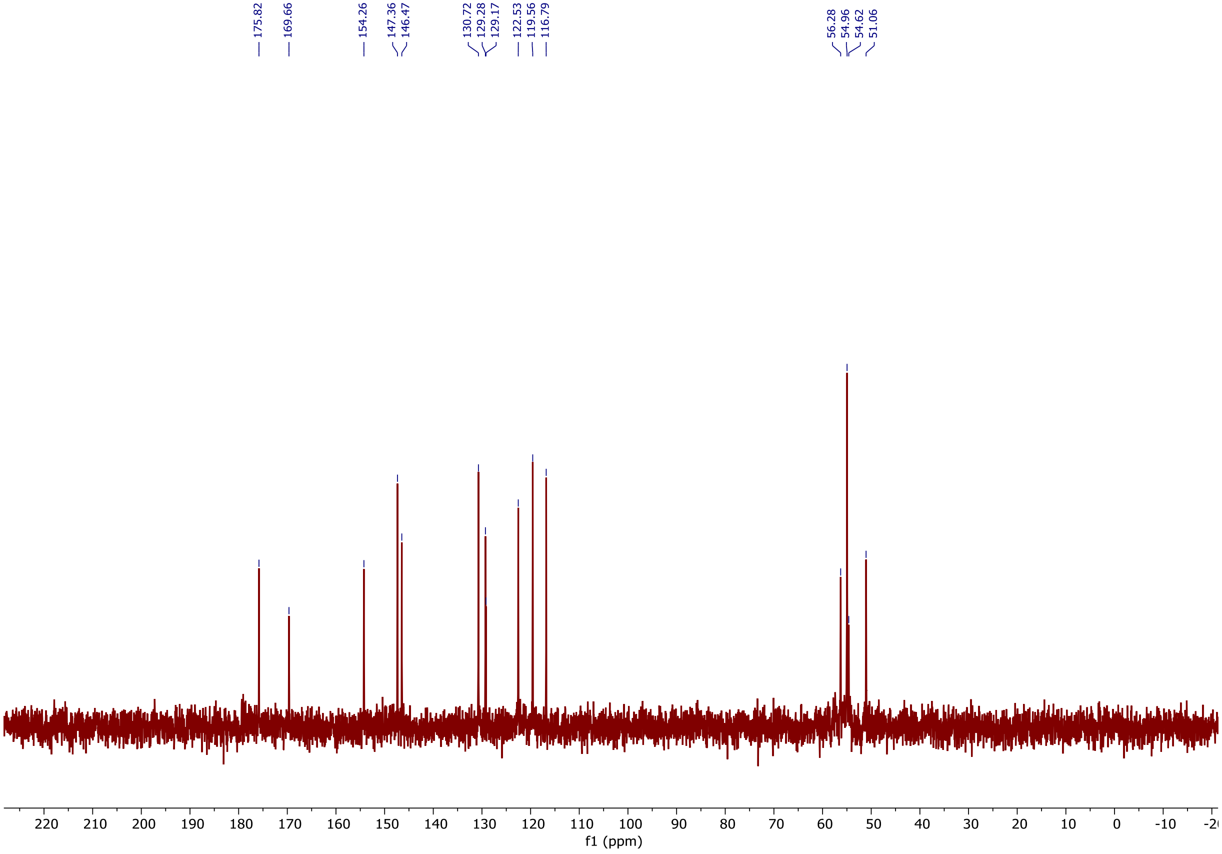

Figure S12. $^{13}C\{^1H\}$ NMR spectrum (D_2O, RT, 75 MHz) of H_5decaox **(7).**

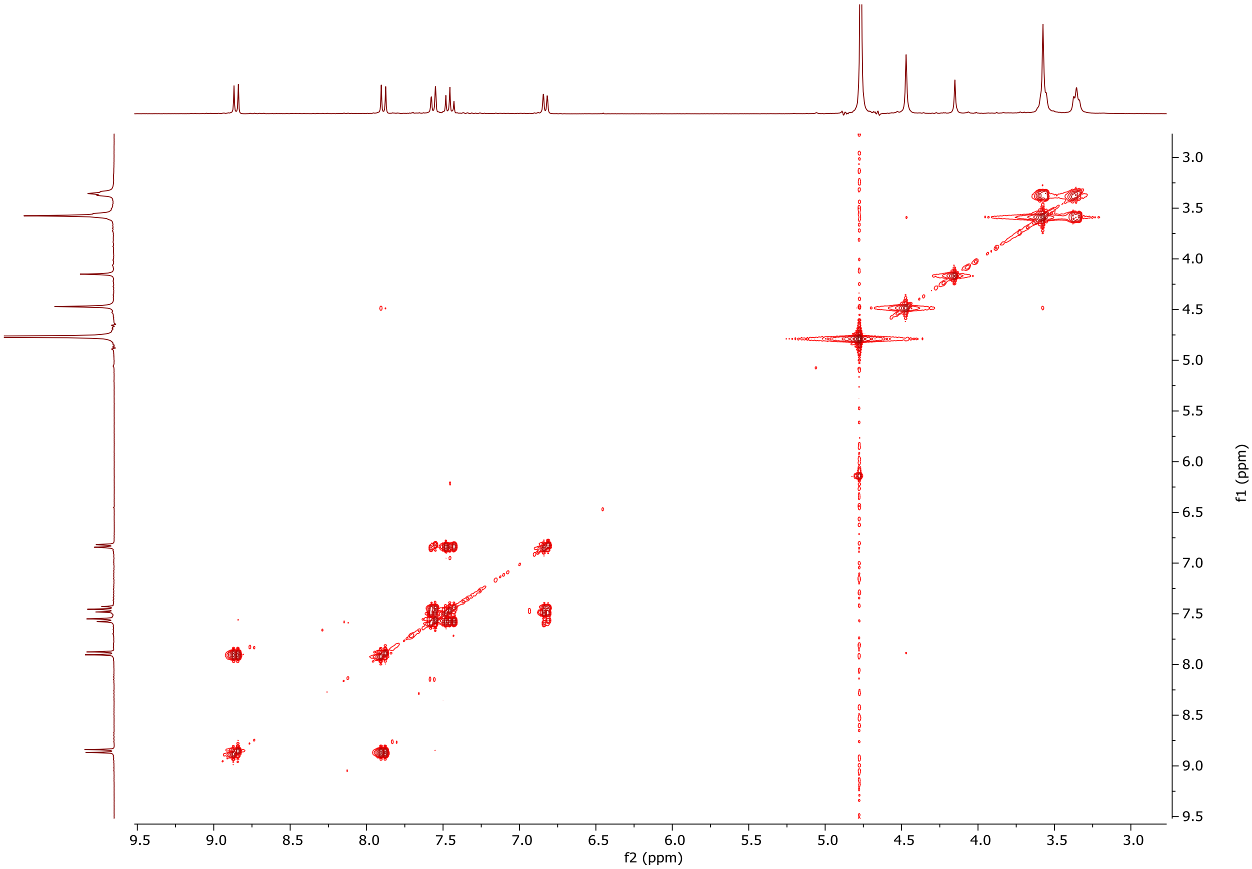

Figure S13. ^{1}H-^{1}H COSY NMR spectrum (D_2O, RT, 300 MHz) of H_5decaox **(7).**

NMR spectra of metal complexes

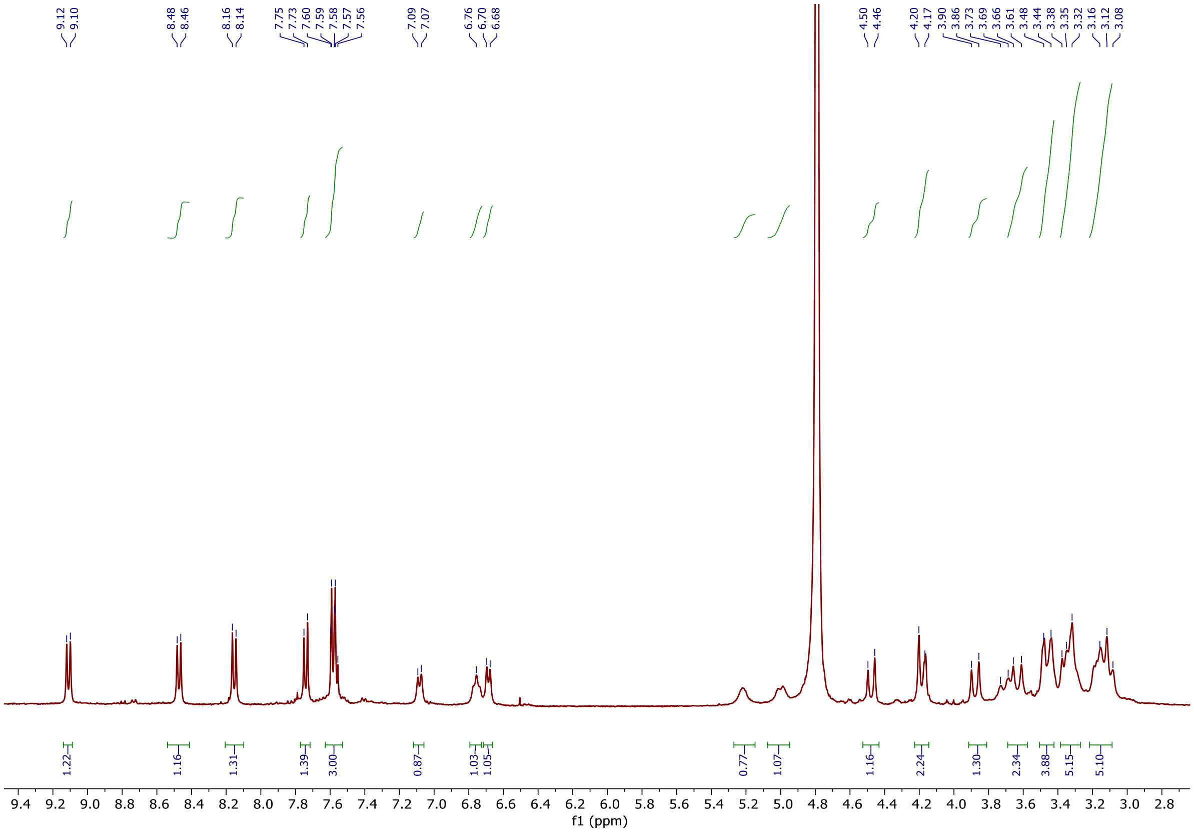

Figure S14. ^{1}H NMR spectrum (D_2O, RT, 400 MHz, pH=6.9) of $[In(H_xdecaox)]^{5-x}$.

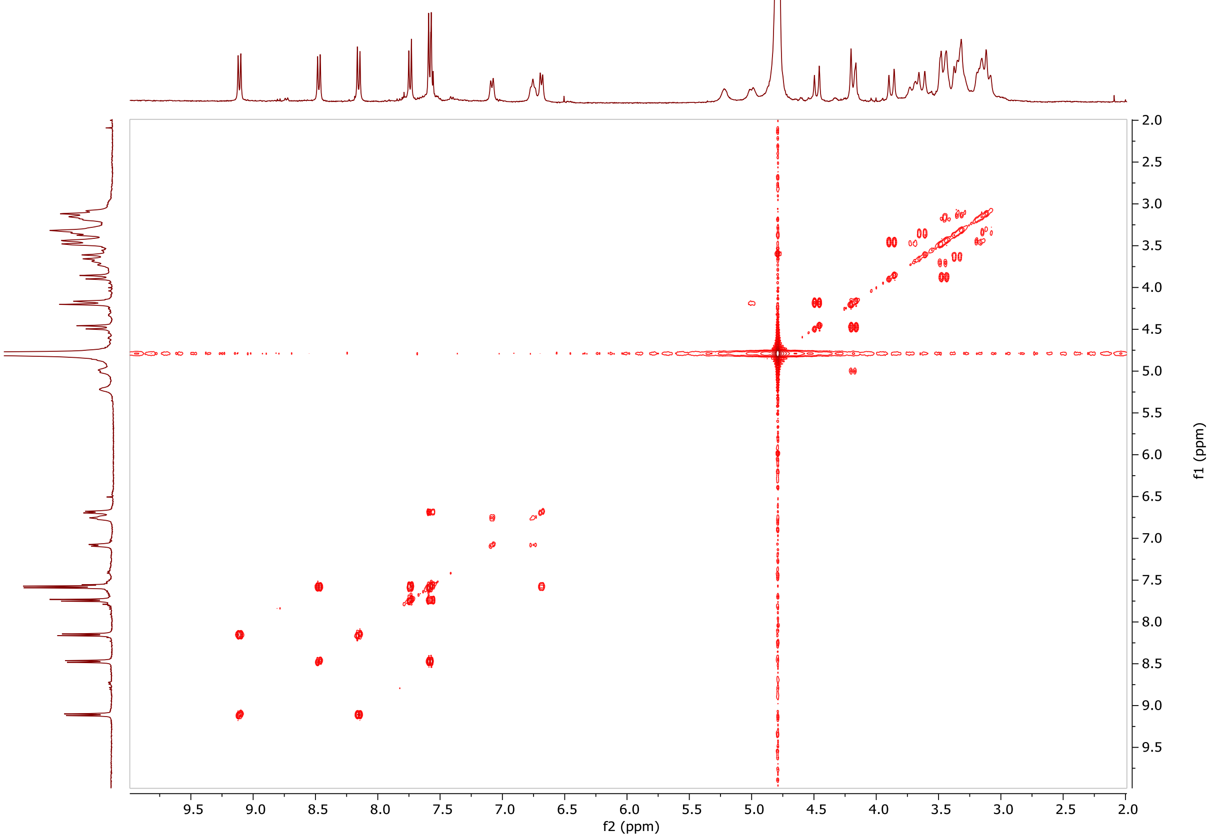

Figure S15. ^{1}H-^{1}H COSY NMR spectrum (D_2O, RT, 400 MHz, pH=6.9) of $[In(H_xdecaox)]^{5-x}$.

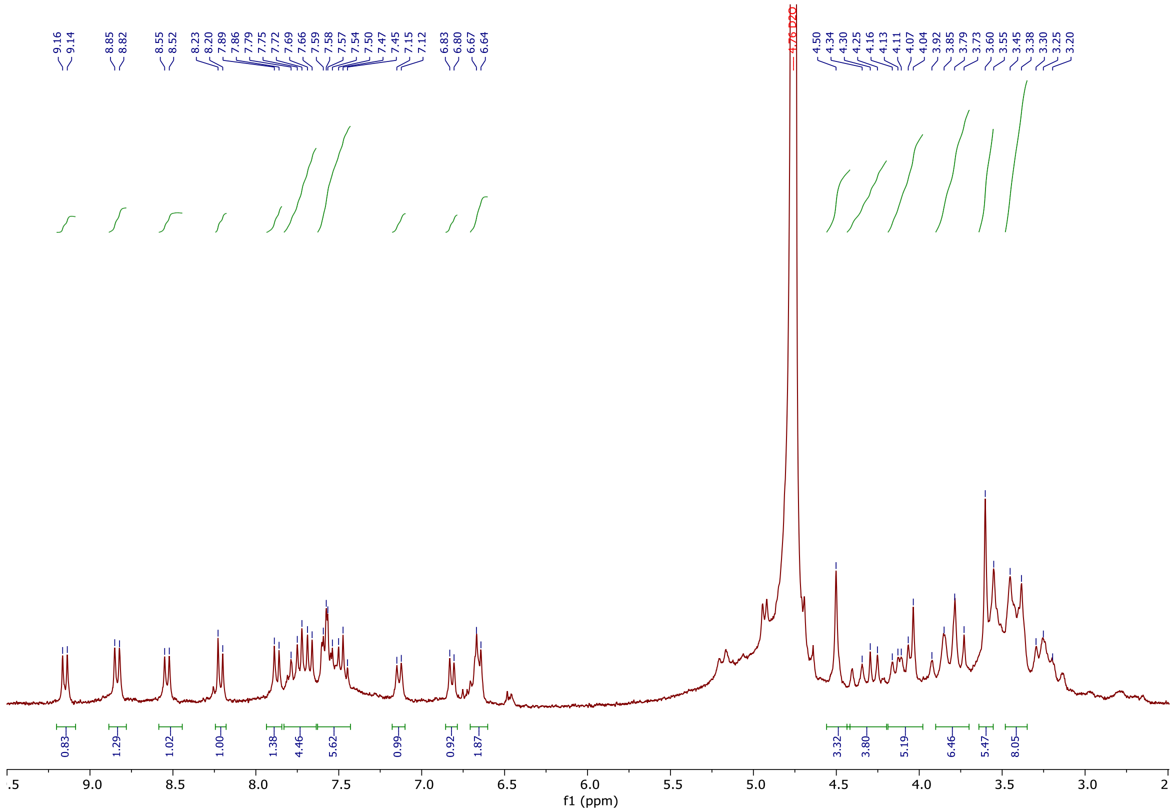

Figure S16. ^{1}H NMR spectrum (D_2O, RT, 300 MHz, pH=2.7) of $[Zr(H_x decaox)]^{5-x}$.

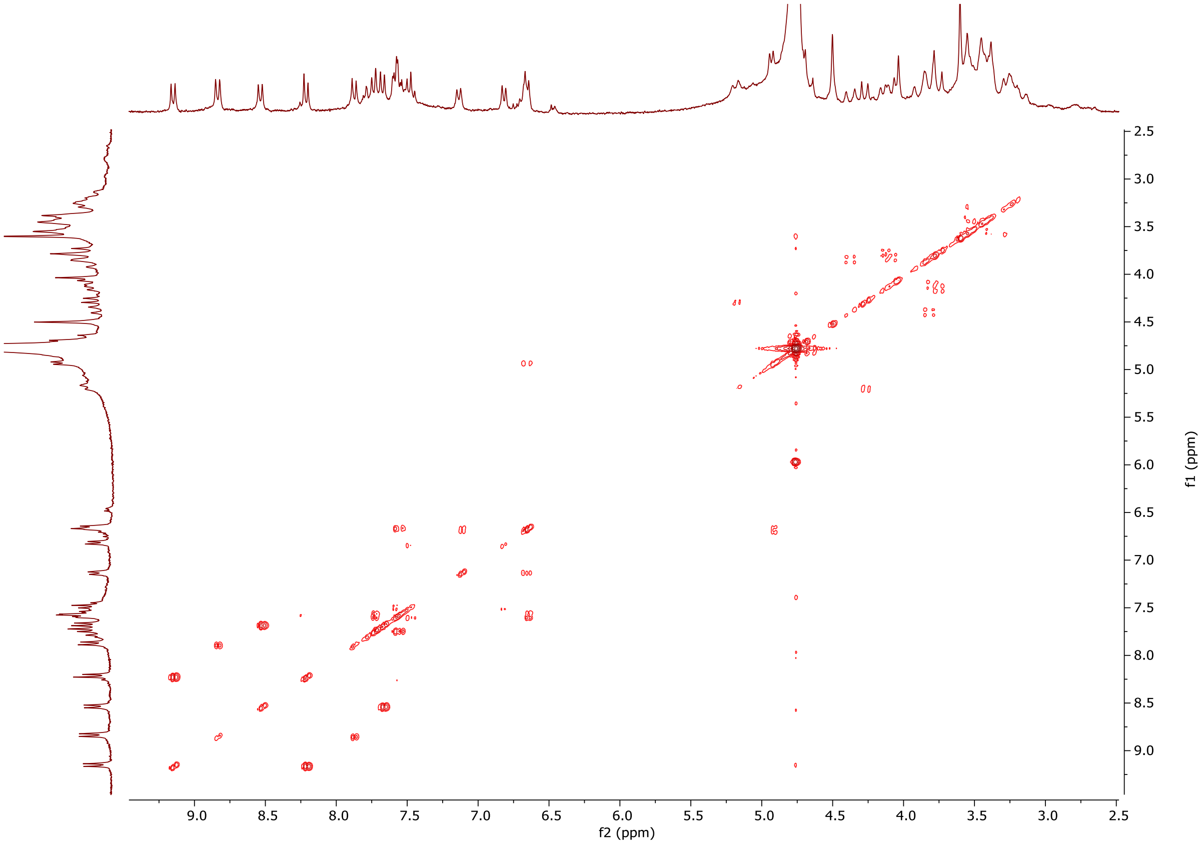

Figure S17. ^{1}H-^{1}H COSY NMR spcetrum (D_2O, RT, 300 MHz, pH=2.7) of $[Zr(Hxdecaox)]^{5-x}$.

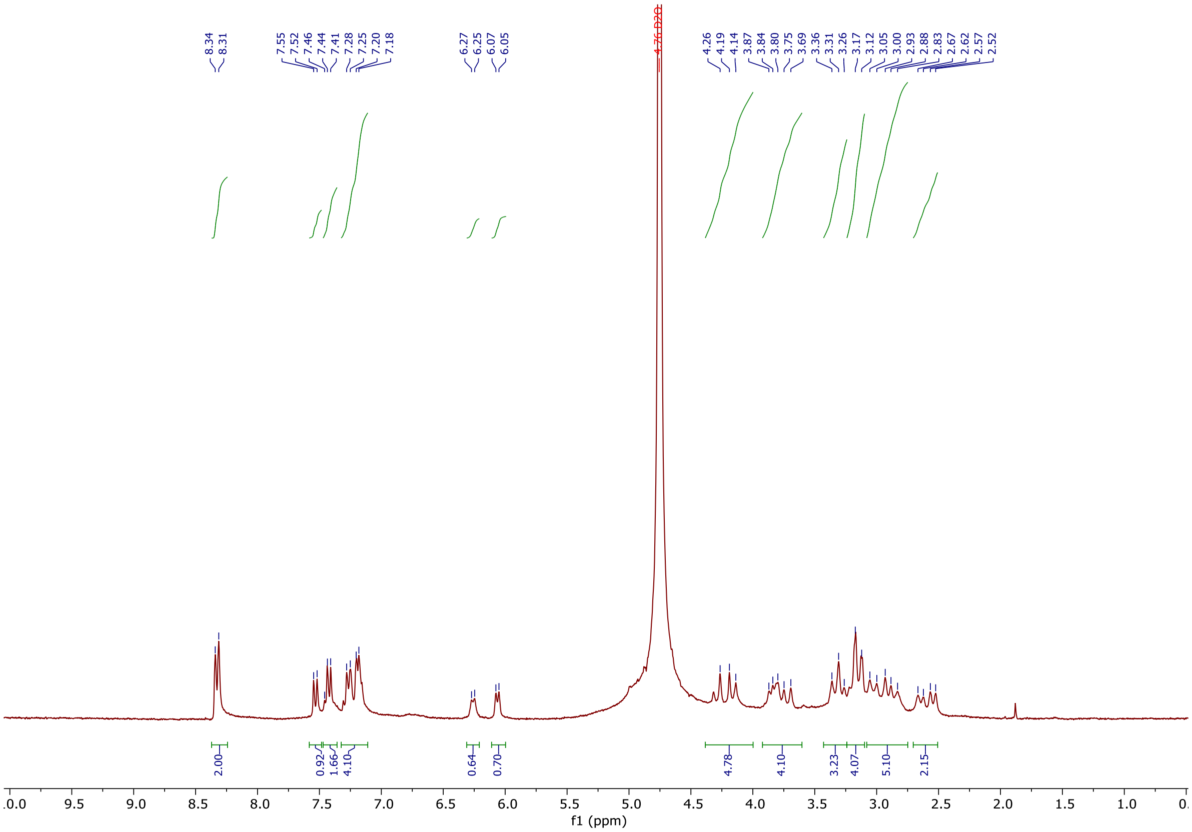

Figure S18. ^1H NMR spectrum (D_2O, RT, 300 MHz, pH=7.3) of $[La(H_x decaox)]^{5-x}$.

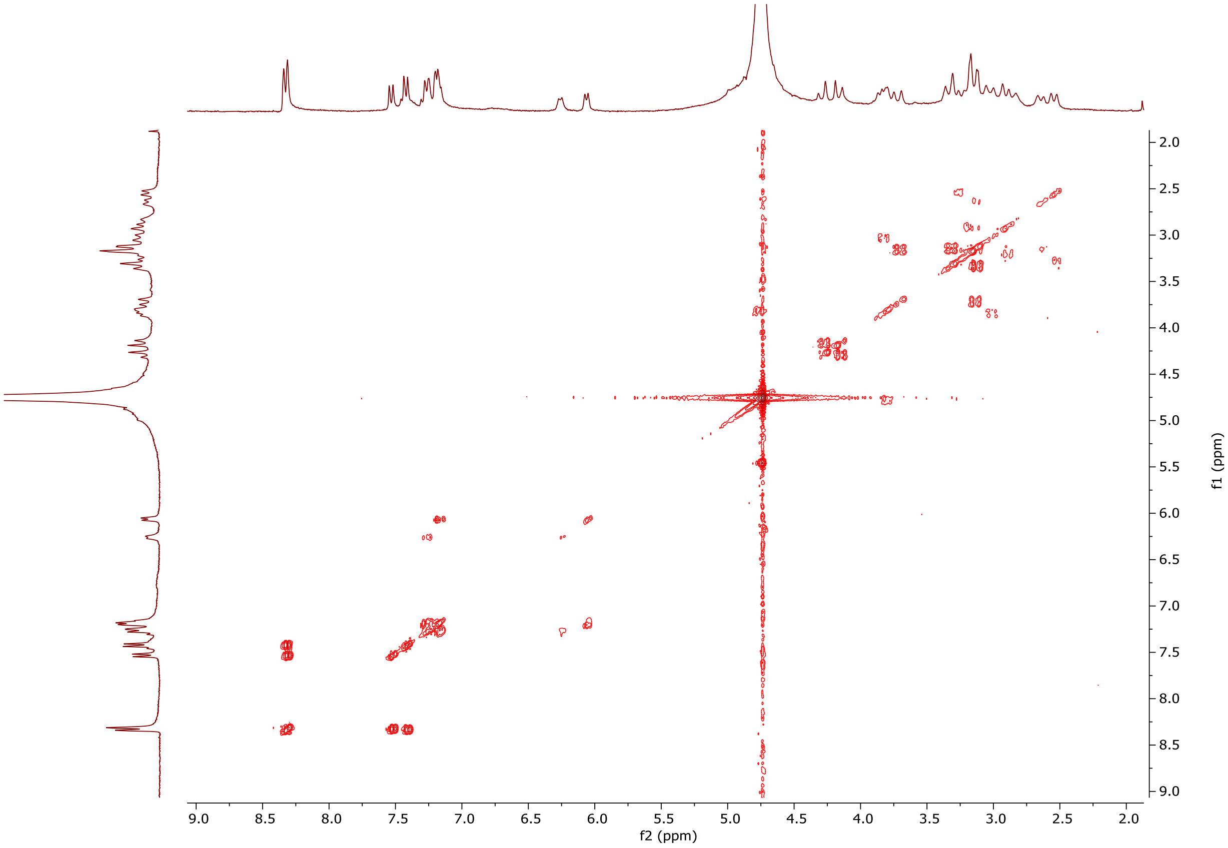

Figure S19. ^1H-^1H COSY NMR spectrum (D_2O, RT, 300 MHz, pH=7.3) of $[La(H_x decaox)]^{5-x}$.

Concentration dependent radiolabeling

Table S1. Radiolabeling yields (%) of H_5decaox at decreasing concentrations.

Ligand Concentration (M)	**[^{111}In]In^{3+}**	**[^{89}Zr]Zr^{4+}**
1×10^{-4}	97.9 ± 0.3	99 ± 1
1×10^{-5}	98 ± 1	96.4 ± 0.4
1×10^{-6}	99 ± 2	89 ± 4
1×10^{-7}	88.8 ± 0.7	21 ± 4
1×10^{-8}	2.0 ± 0.7	ND

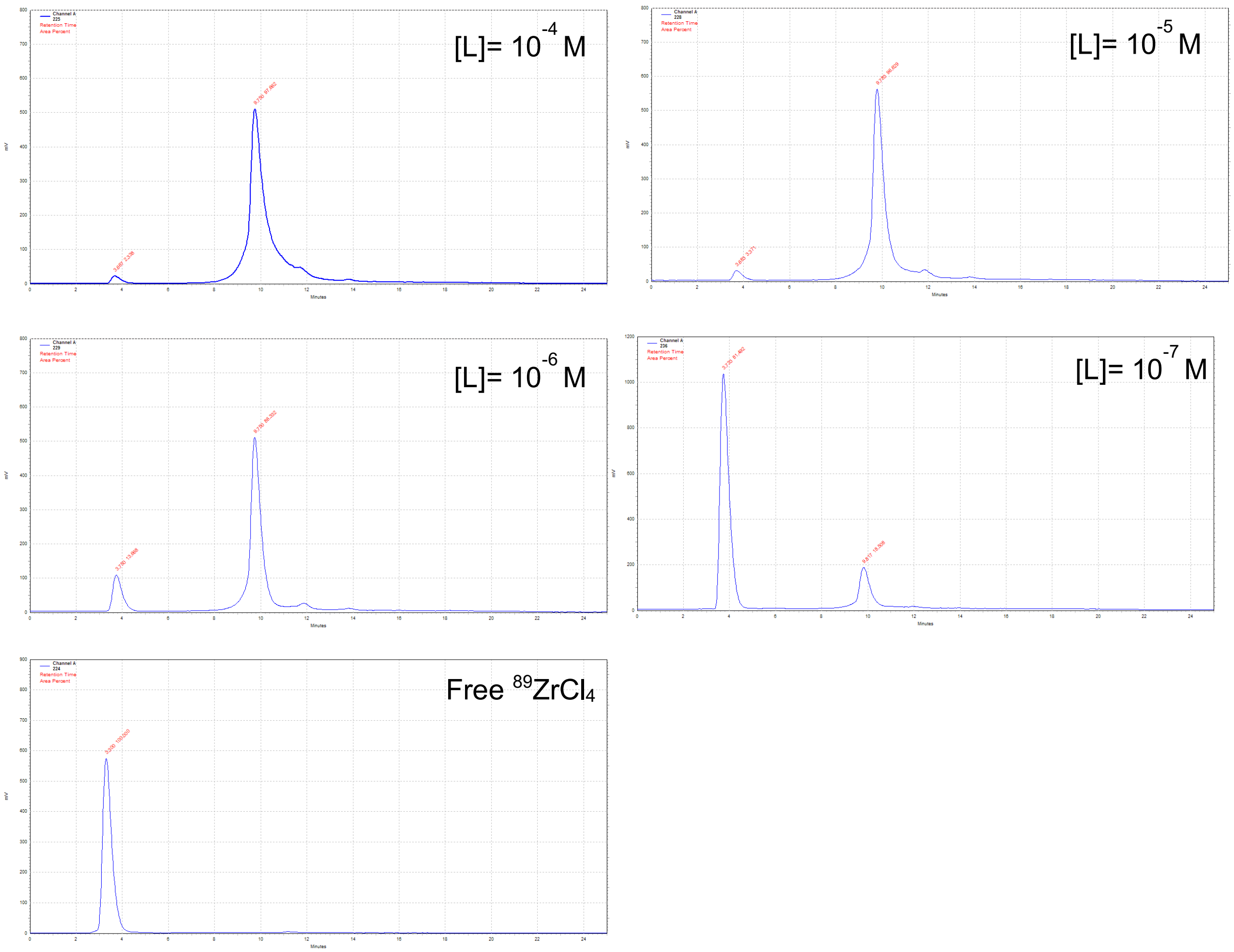

Figure S20. Radio-HPLC traces of [^{89}Zr]Zr(decaox) at decreasing ligand concentrations. Reaction conditions: NaOAc (0.1 M, pH 7) buffer, RT, 30 minutes, 2 MBq of [^{89}Zr]ZrCl$_4$.

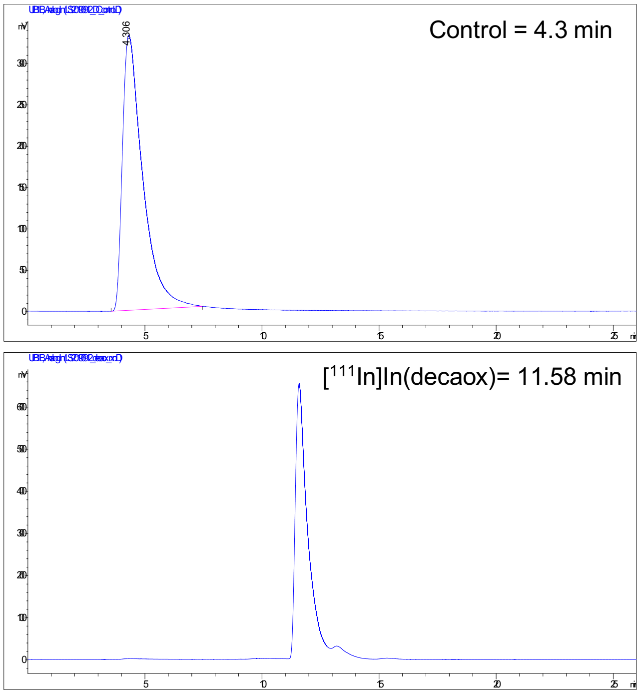

Figure S21. Radio-HPLC traces of free [^{111}In]$InCl_3$ control (top) and [^{111}In]In(decaox) (bottom). Reaction conditions: NaOAc (0.1 M, pH 7) buffer, RT, 30 minutes, 3 MBq of [^{111}In]$InCl_3$.

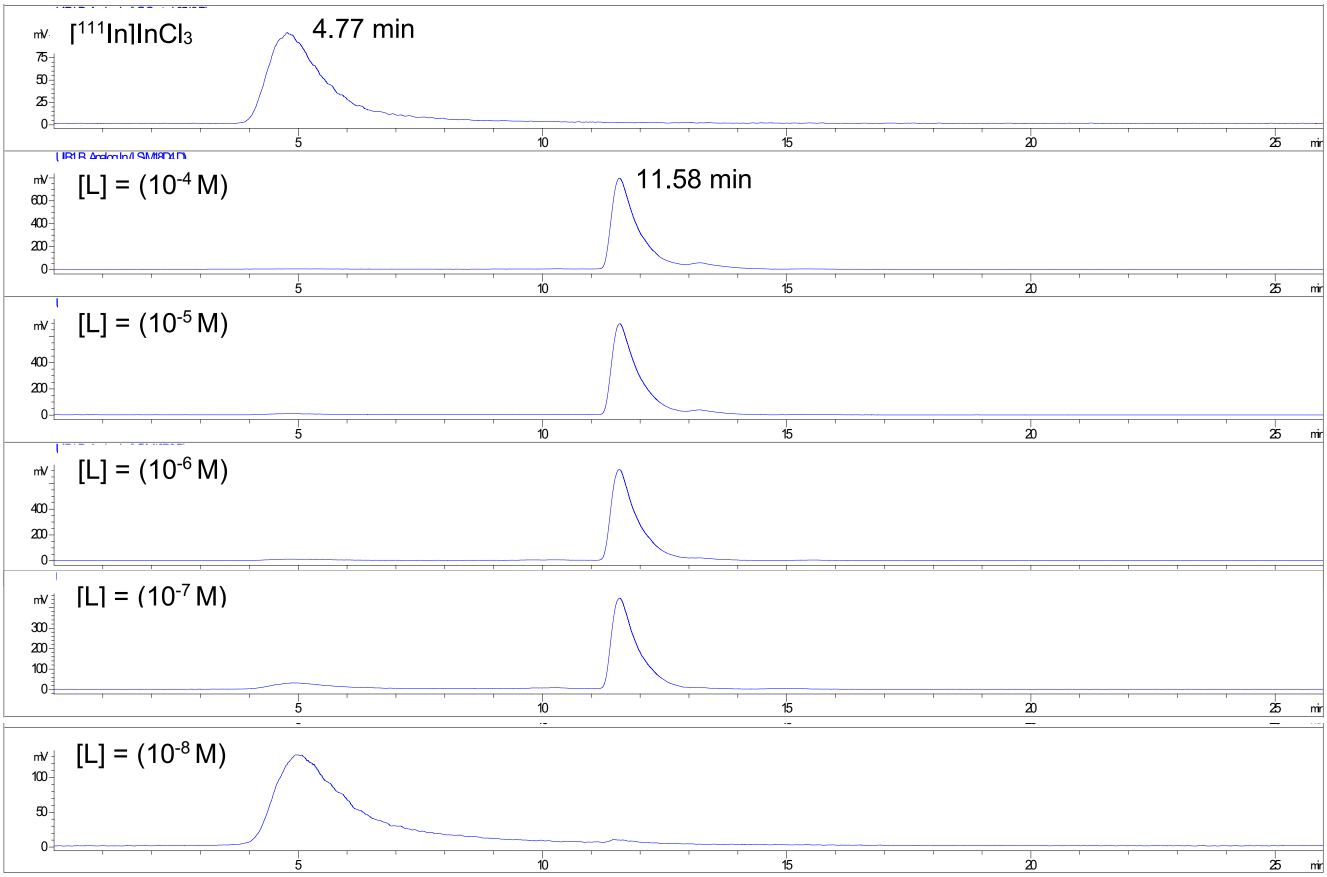

Figure S22. Radio-HPLC traces of [^{111}In]In(decaox) at decreasing ligand concentrations. Reaction conditions: NaOAc (0.1 M, pH 7) buffer, RT, 30 minutes, 3 MBq of [^{111}In]$InCl_3$.

Solution thermodynamics

Ligand protonation constants

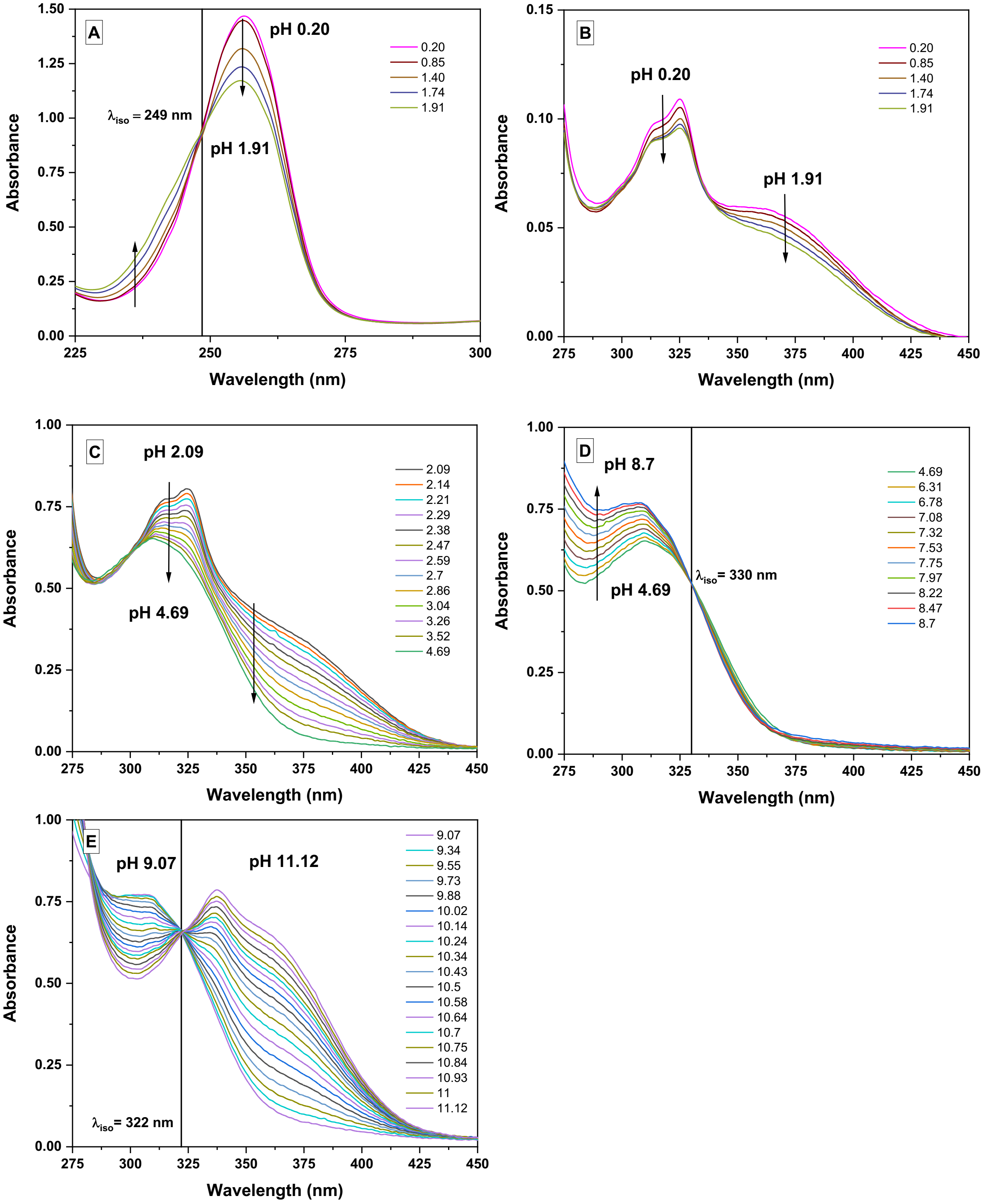

Figure S23. Representative spectra of H_5decaox during (A/B) acidic in-batch UV spectrophotometric titration [L] = 2.25×10^{-5} M, T = 25 ℃, l = 1 cm, *I* = 0.16 M NaCl when possible; (C-E) combined UV-potentiometric titration [L] = 9.62×10^{-4} M, T = 25 ℃, l = 0.2 cm, *I* = 0.16 M NaCl.

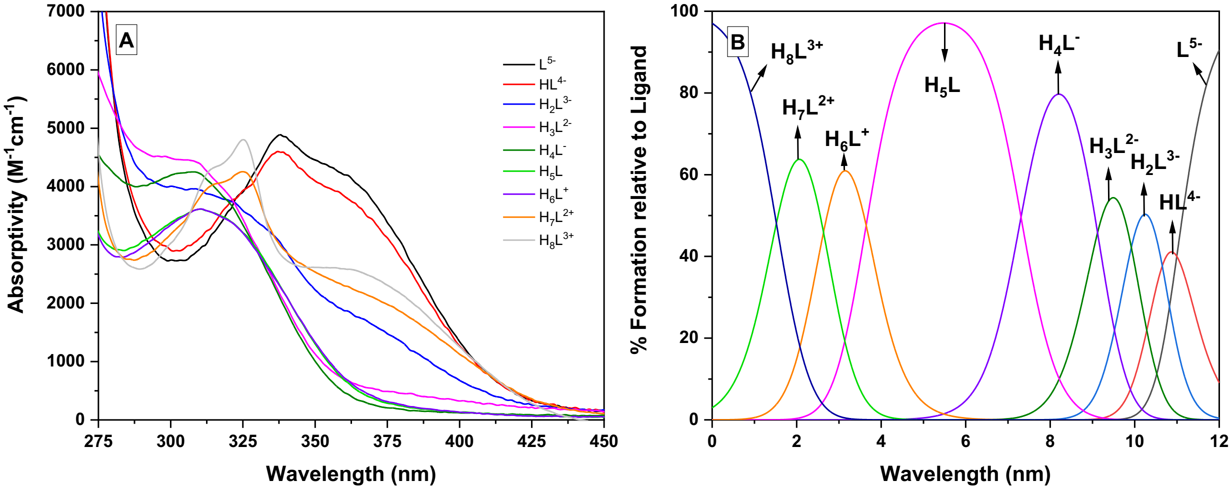

Figure S24. (A) Electronic spectra of the nine absorbing species in H_5decaox; (B) speciation plot of H_5decaox calculated with protonation constants in Table 1, [H_5decaox] = 1 × 10^{-4} M.

Metal complexation with Zr^{4+}, In^{3+} and La^{3+}

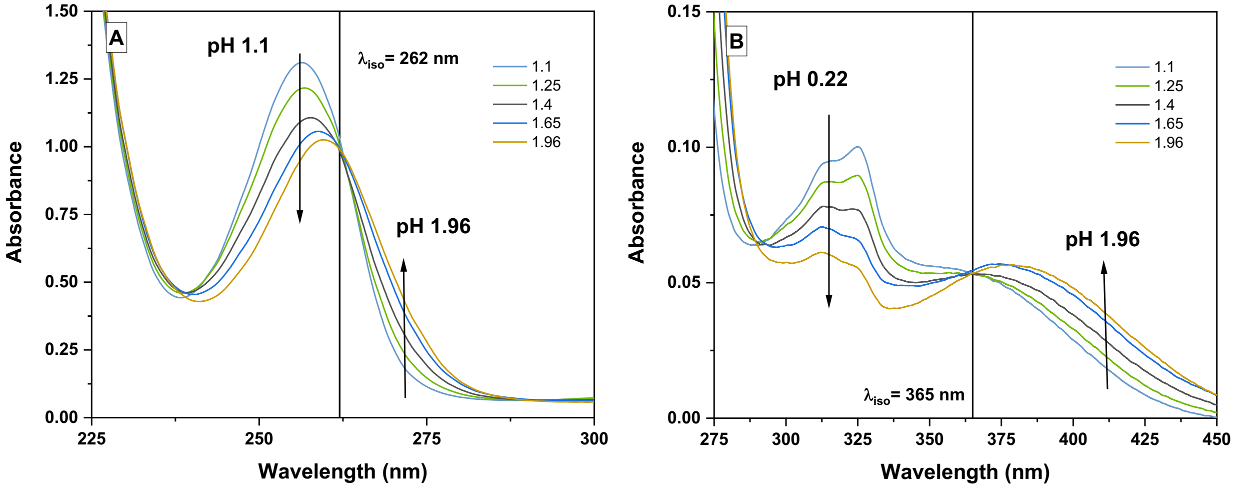

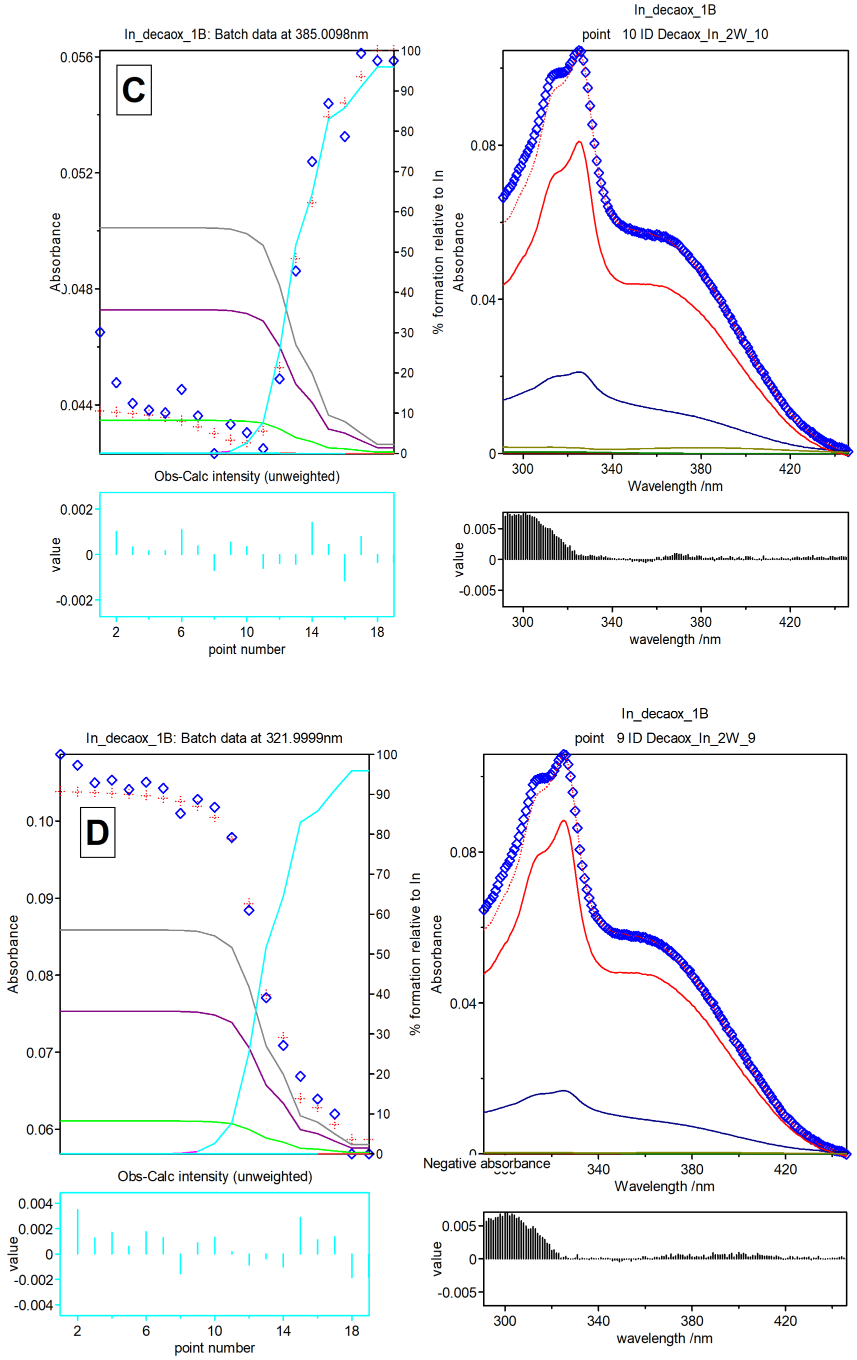

Figure S25. Representative spectra of In^{3+}-H$_5$decaox during (A-B) UV-acidic batch titration [In^{3+}] = [L] = 2.25 × 10^{-5} M, T = 25 °C, l = 1 cm, *I* = 0.16 M NaCl; (C-D) Change of absorbance in the same UV-acidic batch experiment at 322 nm and 385 nm; blue dots are original data points and red dots represents the fit versus data points (upper and lower left). Obtained (blue) and fitted (red) spectra for pH = 0.99 and 0.85 specific data points (upper and lower right).

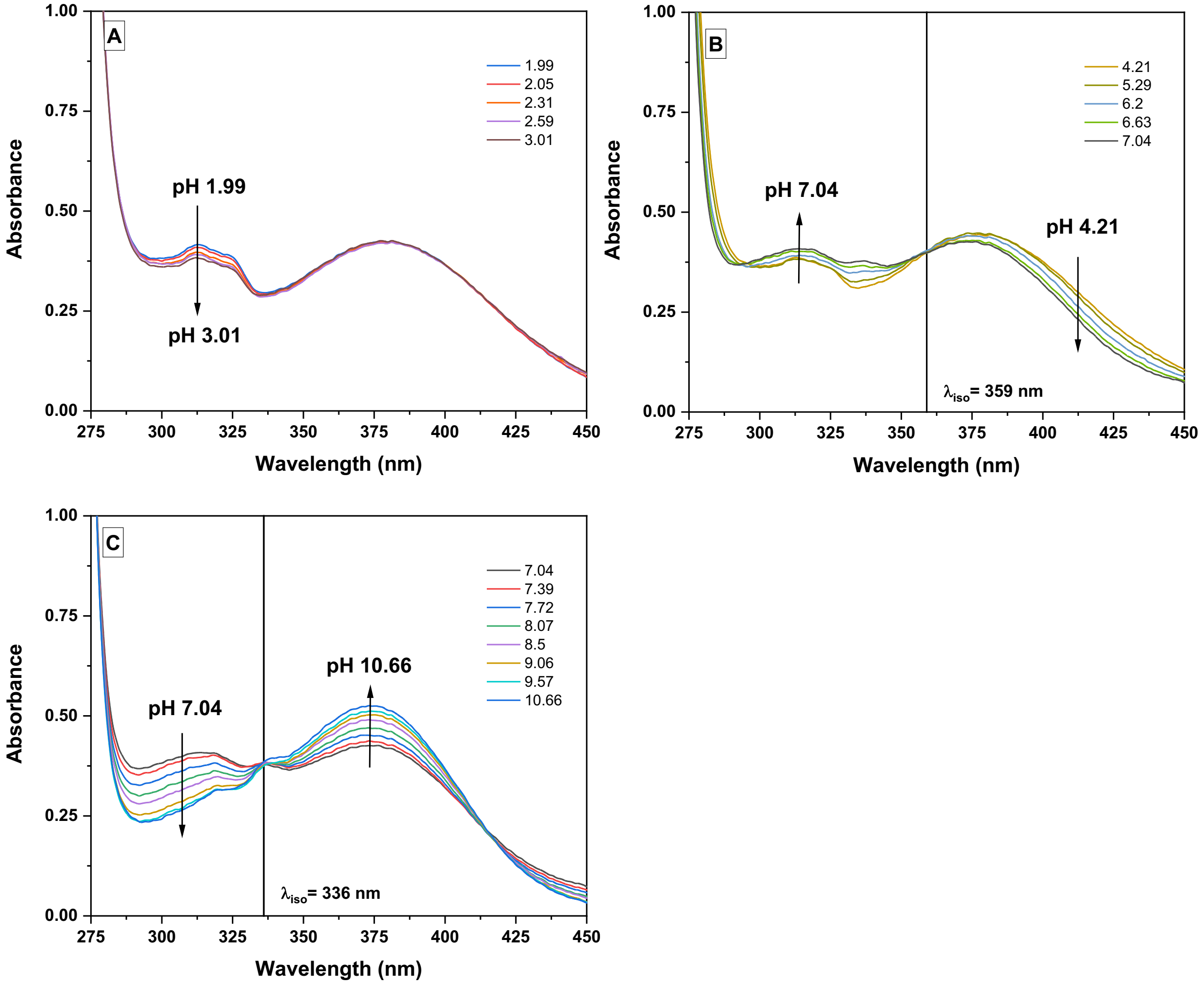

Figure S26. Representative spectra of In^{3+}-H$_5$decaox during (A-C) UV-potentiometric titration [In^{3+}] = [L] = 7.67 × 10^{-4} M, T = 25 ℃, l = 0.2 cm, I = 0.16 M NaCl.

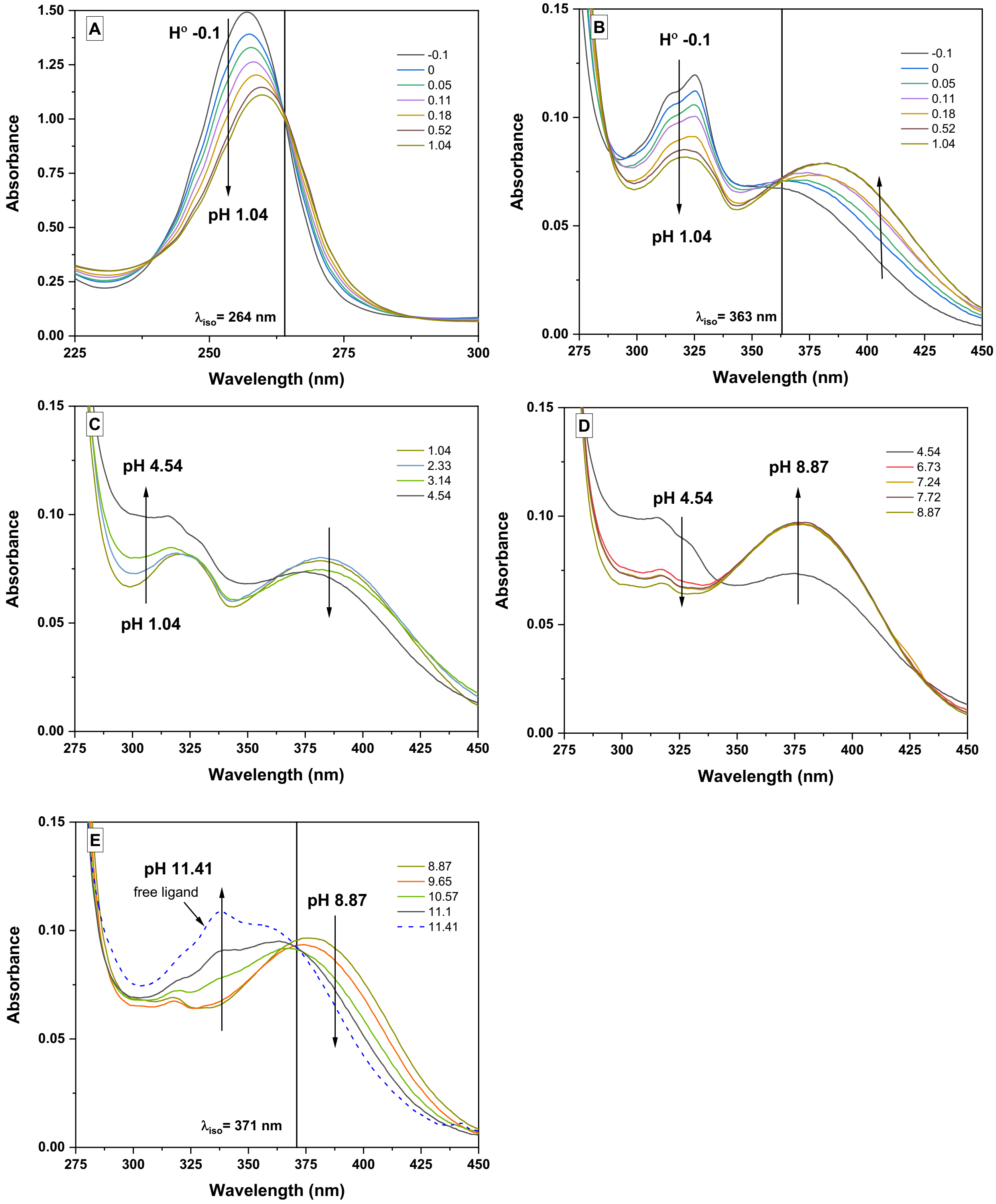

Figure S27. Representative spectra of Zr^{4+}-H$_5$decaox during (A-E) UV-batch titration [Zr^{4+}] = [L] = 2.0 × 10^{-5} M, T = 25 °C, l = 1 cm, *I* = 0.16 M NaCl.

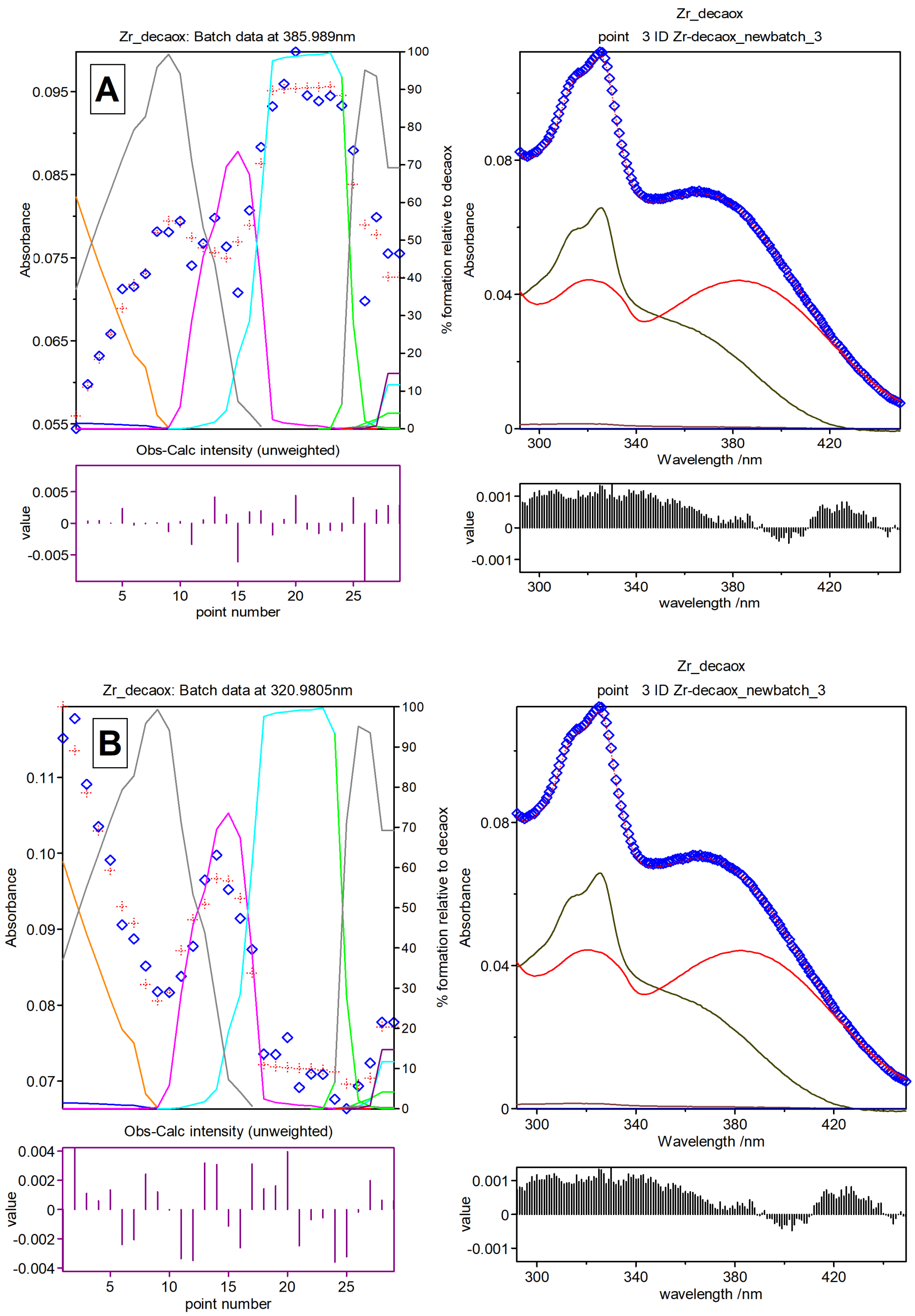

Figure S28. Change of absorbance of Zr^{4+}-H_5decaox during the UV-acidic batch experiment at 321 nm and 386 nm; blue dots are original data points and red dots represents the fit versus data points (upper and lower left). Obtained (blue) and fitted (red) spectra for pH = 0 specific data point (upper and lower right).

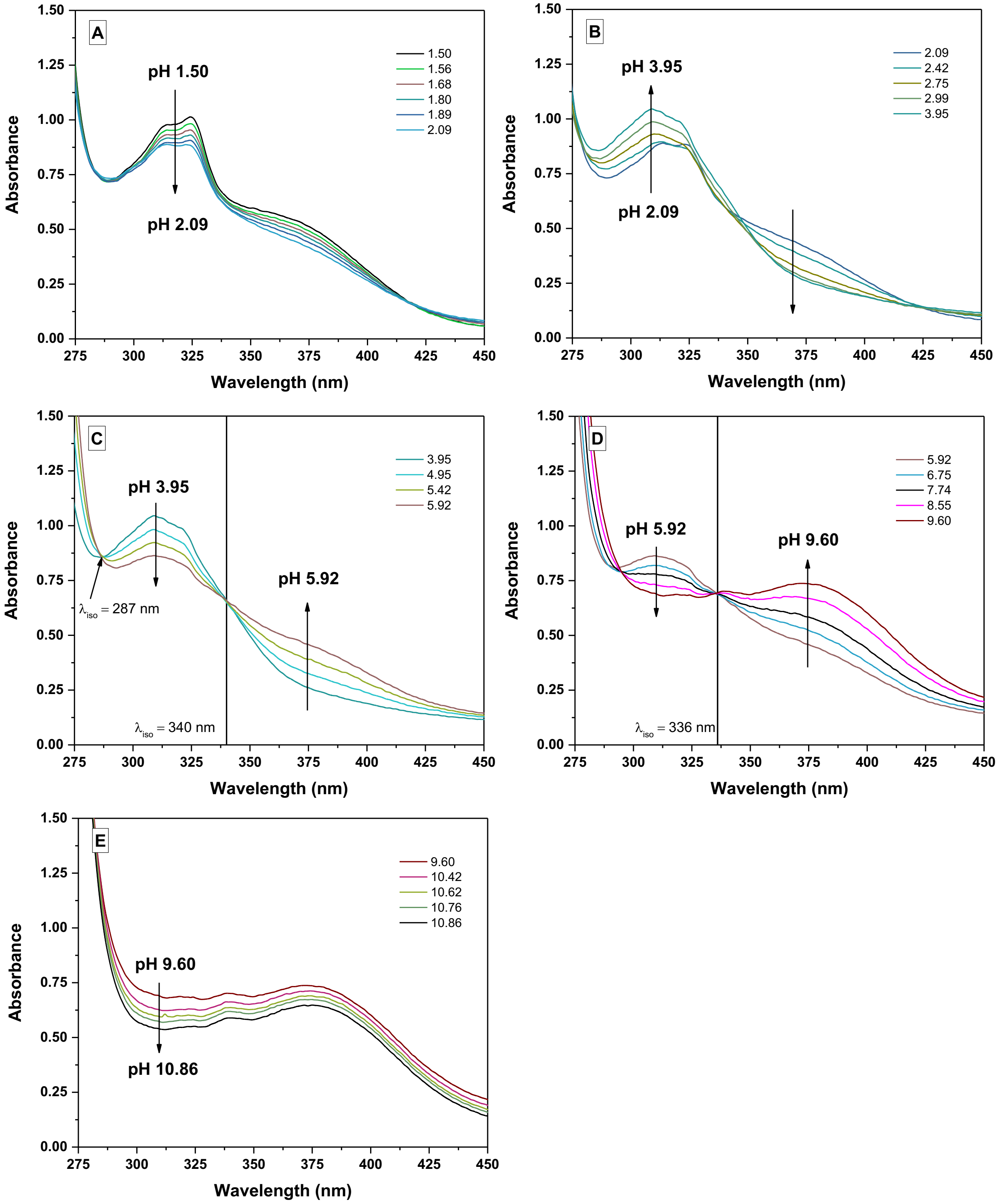

Figure S29. Representative spectra of La^{3+}-H_5decaox during (A-E) combined UV-potentiometric titration $[La^{3+}] = [L] = 8.31 \times 10^{-4}$ M, T = 25 °C, l = 0.2 cm, I = 0.16 M NaCl.

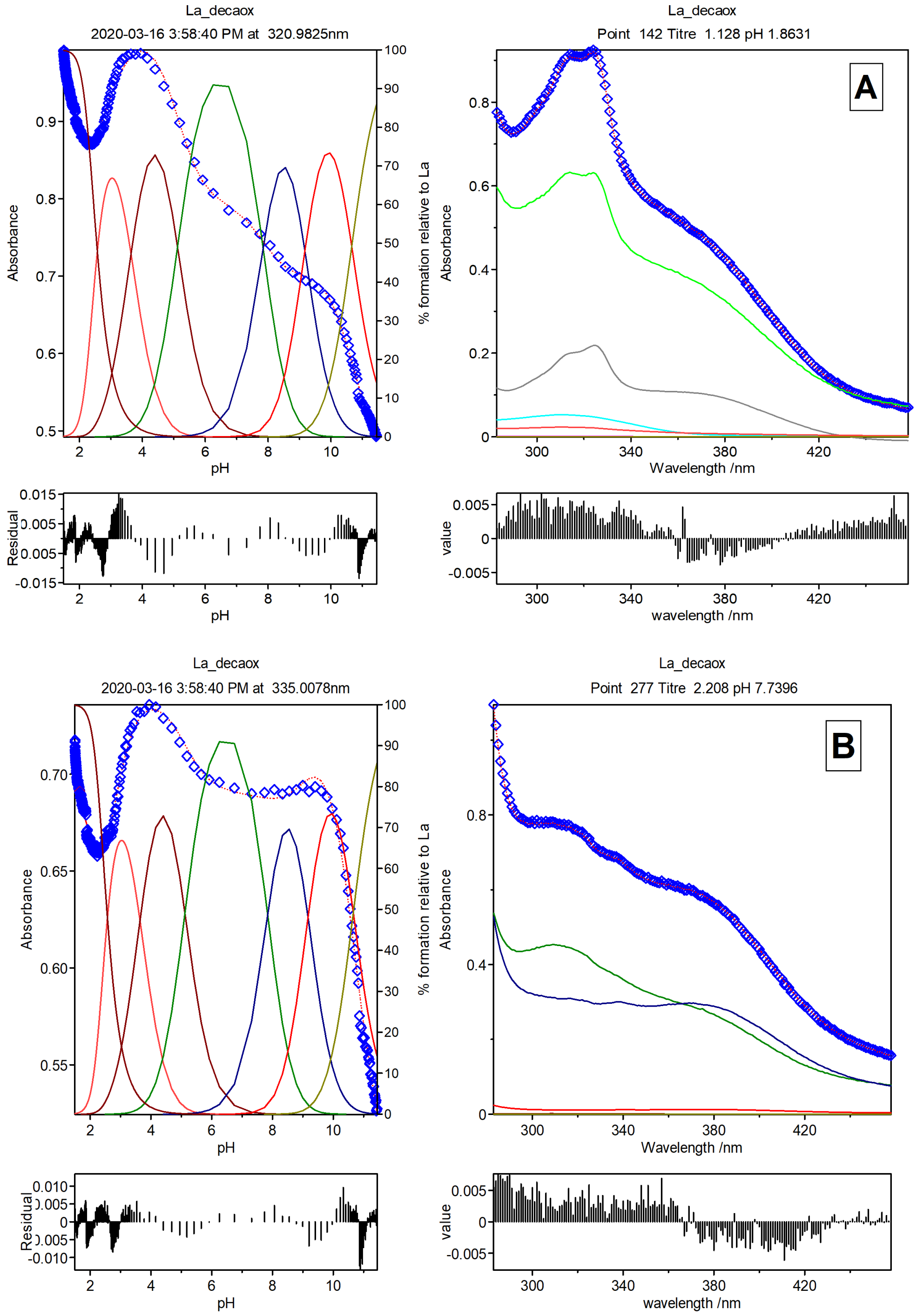

Figure S30. Change of absorbance of La^{3+}-H$_5$decaox during the UV-potentiometric experiment at 321 nm and 335 nm; blue dots are original data points and red dots represents the fit versus data points (upper and lower left). Obtained (blue) and fitted (red) spectra for pH = 1.86 and 7.74 specific data points (upper and lower right).

Density Functional Theory (DFT) calculations

$[In(decaox)]^{2-}$ A (capped octahedral)

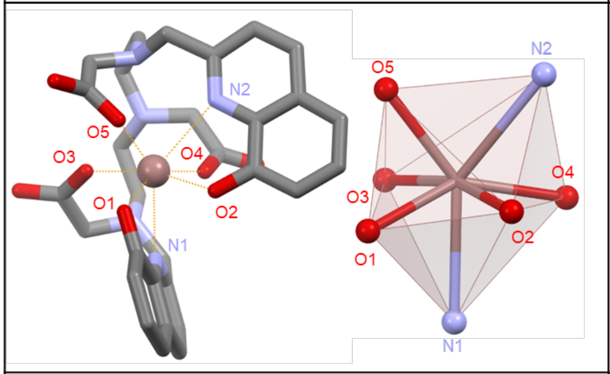

$[In(decaox)]^{2-}\cdot 4H_2O$ A (capped octahedral)

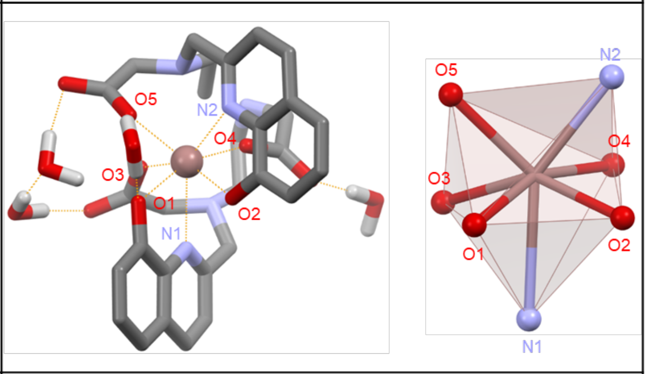

$[In(decaox)]^{2-}$ B (pentagonal bipyramidal)

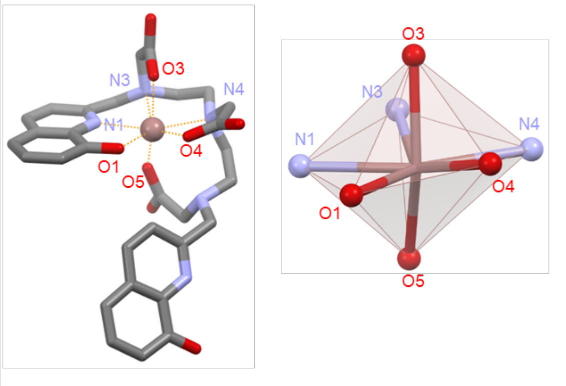

$[In(decaox)]^{2-}\cdot 4H_2O$ B (pentagonal bipyramidal)

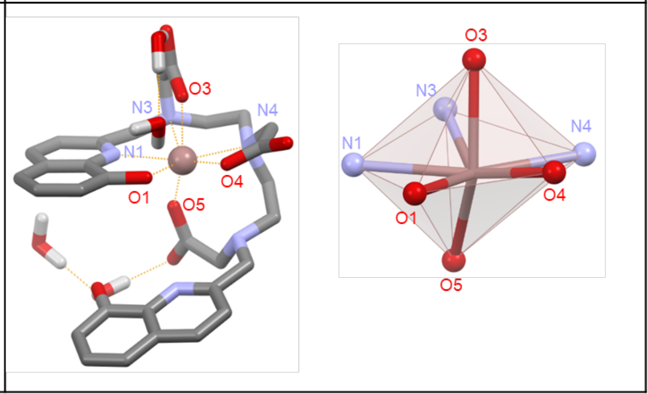

Figure S31. DFT calculated $[In(decaox)]^{2-}$ structures.

Table S2. Bond lengths from DFT-calculated $[In(decaox)]^{2-}$ structures

	M-O (ligand) distances (Å)					**M-N (Ligand) Distances (Å)**					
	COOH	COOH	COOH	Ox 1	Ox 2	Ox 1	Ox 2	3° N	3° N	3° N	Free Energy
	O3	**O4**	**O5**	**O1**	**O2**	**N1**	**N2**	**N3**	**N4**	**N5**	**(Ha)**
$[In(decaox)]^{2-}$A	2.17	2.163	2.196	2.203	2.179	2.602	2.761	3.366	3.571	3.41	-2224.178
$[In(decaox)]^{2-}$B	2.187	2.185	2.163	2.184	out	2.329	out	2.561	2.436	3.287	-2224.210
$[In(decaox)]^{2-}$A·4H₂O	2.194	2.169	2.277	2.206	2.186	2.676	2.4	3.685	4.546	2.921	-2529.678
$[In(decaox)]^{2-}$B·4H₂O	2.186	2.185	2.176	2.203	out	2.33	out	2.572	2.413	3.158	-2529.709

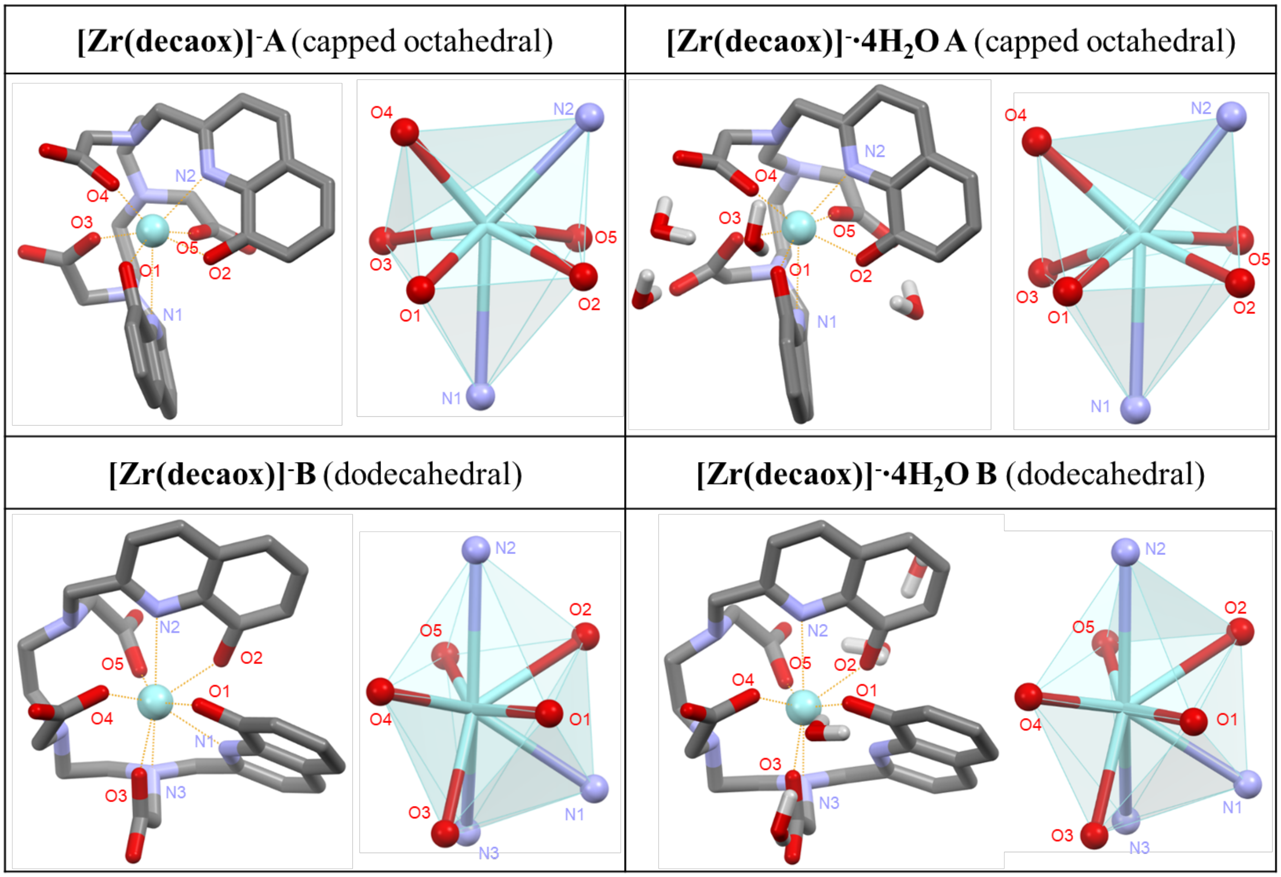

$[Zr(decaox)]^{-}$A (capped octahedral)

$[Zr(decaox)]^{-}\cdot 4H_2O$ A (capped octahedral)

$[Zr(decaox)]^{-}$B (dodecahedral)

$[Zr(decaox)]^{-}\cdot 4H_2O$ B (dodecahedral)

Figure S32. DFT calculated $[Zr(decaox)]^{-}$ structures.

Table S3. Bond lengths from DFT-calculated $[Zr(decaox)]^{-}$ structures

	M-O (ligand) distances (Å)					**M-N (Ligand) Distances (Å)**					
	COOH	COOH	COOH	Ox 1	Ox 2	Ox 1	Ox 2	3° N	3° N	3° N	Free Energy
	O3	**O4**	**O5**	**O1**	**O2**	**N1**	**N2**	**N3**	**N4**	**N5**	**(Ha)**
$[Zr(decaox)]^{-}$A	2.082	2.074	2.147	2.085	2.139	2.728	2.448	3.66	3.768	2.997	-2081.153
$[Zr(decaox)]^{-}$B	2.22	2.136	2.123	2.158	2.231	2.38	2.659	2.675	2.829	3.249	-2081.148
$[Zr(decaox)]^{-}$A·4H_2O	2.098	2.084	2.195	2.108	2.148	2.642	2.391	3.741	4.507	2.75	-2386.646
$[Zr(decaox)]^{-}$B·4H_2O	2.208	2.121	2.122	2.175	2.267	2.382	2.671	2.657	2.79	3.253	-2386.651

$[La(decaox)]^{2-}$ A (capped triangular cupola) | **$[La(decaox)]^{2-}\cdot 4H_2O$ A** (capped triangular cupola)

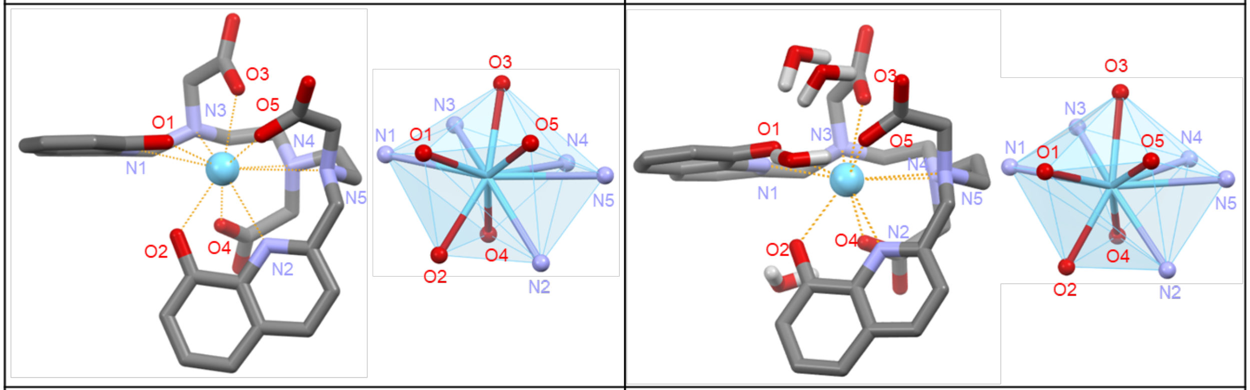

$[La(decaox)]^{2-}$ B (sphenocorona) | **$[La(decaox)]^{2-}\cdot 4H_2O$ B** (sphenocorona)

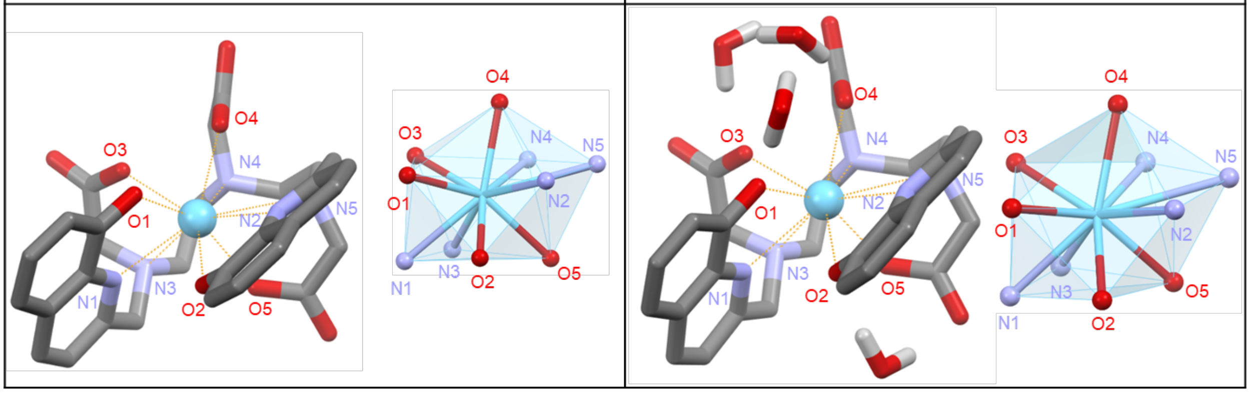

Figure S33. DFT calculated $[La(decaox)]^{2-}$ structures.

Table S4. Bond lengths from DFT-calculated $[La(decaox)]^{2-}$ structures

	M-O (ligand) distances (Å)					**M-N (Ligand) Distances (Å)**					
	COOH **O3**	COOH **O4**	COOH **O5**	Ox 1 **O1**	Ox 2 **O2**	Ox 1 **N1**	Ox 2 **N2**	3° N **N3**	3° N **N4**	3° N **N5**	Free Energy **(Ha)**
$[La(decaox)]^{2-}$A	2.483	2.502	2.545	2.474	2.481	2.828	2.797	3.104	3.146	3.096	-2469.802
$[La(decaox)]^{2-}$B	2.562	2.477	2.483	2.504	2.58	2.666	2.835	2.888	2.925	3.079	-2469.797
$[La(decaox)]^{2-}$A·$4H_2O$	2.484	2.506	2.565	2.592	2.469	2.816	2.774	3.044	3.123	3.080	-2775.883[a]
$[La(decaox)]^{2-}$B·$4H_2O$	2.569	2.546	2.442	2.516	2.605	2.695	2.811	2.88	2.985	3.099	-2775.884[a]

[a] Potential energy (RPBE1PBE energy calculation)